remote sensing

MDPI

Article

Performance Assessment of Balloon-Borne Trace Gas Sounding with the Terahertz Channel of TELIS

Jian Xu [1,*], Franz Schreier [1], Gerald Wetzel [2], Arno de Lange [3,†], Manfred Birk [1], Thomas Trautmann [1], Adrian Doicu [1] and Georg Wagner [1]

1 Remote Sensing Technology Institute (IMF), German Aerospace Center (DLR), 82234 Oberpfaffenhofen, Germany; franz.schreier@dlr.de (F.S.); manfred.birk@dlr.de (M.B.); thomas.trautmann@dlr.de (T.T.); adrian.doicu@dlr.de (A.D.); georg.wagner@dlr.de (G.W.)

2 Institute of Meteorology and Climate Research (IMK), Karlsruhe Institute of Technology (KIT), 76021 Karlsruhe, Germany; gerald.wetzel@kit.edu

3 Netherlands Institute for Space Research (SRON), 3584 CA Utrecht, The Netherlands; a.de.lange@airbusds.nl

* Correspondence: jian.xu@dlr.de; Tel.: +49-8153-28-3353

† Current address: Airbus Defence and Space Netherlands, Mendelweg 30, 2333 CS Leiden, The Netherlands.

Received: 22 December 2017; Accepted: 16 February 2018; Published: 19 February 2018

Abstract: Short-term variations in the atmospheric environment over polar regions are attracting increasing attention with respect to the reliable analysis of ozone loss. Balloon-borne remote sensing instruments with good vertical resolution and flexible sampling density can act as a prototype to overcome the potential technical challenges in the design of new spaceborne atmospheric sensors and represent a valuable tool for validating spaceborne observations. A multi-channel cryogenic heterodyne spectrometer known as the TErahertz and submillimeter LImb Sounder (TELIS) has been developed. It allows limb sounding of the upper troposphere and stratosphere (10–40 km) within the far infrared (FIR) and submillimeter spectral regimes. This paper describes and assesses the performance of the profile retrieval scheme for TELIS with a focus on the ozone (O_3), hydrogen chloride (HCl), carbon monoxide (CO), and hydroxyl radical (OH) measured during three northern polar campaigns in 2009, 2010, and 2011, respectively. The corresponding inversion diagnostics reveal that some forward/instrument model parameters play important roles in the total retrieval error. The accuracy of the radiometric calibration and the spectroscopic knowledge has a significant impact on retrieval at higher altitudes, whereas the pointing accuracy dominates the total error at lower altitudes. The TELIS retrievals achieve a vertical resolution of $\sim$2–3 km through most of the stratosphere below the balloon height. Dominant water vapor (H_2O) contamination and low abundances of the target species reduce the retrieval sensitivity at the lowermost altitudes measured by TELIS. An extensive comparison shows that the TELIS profiles are consistent with profiles obtained by other limb sounders. The comparison appears to be very promising, except for discrepancies in the upper troposphere due to numerical regularization. This study not only consolidates the validity of balloon-borne TELIS FIR measurements, but also demonstrates the scientific relevance and technical feasibility of terahertz limb sounding of the stratosphere.

Keywords: far infrared spectroscopy; balloon-borne limb sounding; stratospheric trace gases; inverse problems; TELIS

1. Introduction

Studies on the changes in atmospheric trace gas abundances in the stratosphere are valuable for research relevant to climate change and ozone depletion. Owing to the formation of polar stratospheric clouds (PSCs) and the indications of the ozone hole, the lower stratosphere is of great interest during

winter and spring times. The temporal variability of relevant geophysical parameters and associated chemical processes requires an optimal vertical resolution of the measured data.

Far infrared (FIR) and submillimeter limb emission sounding is a widely used remote sensing technique for monitoring of the Earth's atmosphere. The spectroscopic properties of water vapor (H_2O), ozone (O_3), oxygen (O_2), and many minor constituents in this spectral interval introduce the possibility of measuring the distribution of these molecules in the atmosphere [1]. Atmospheric limb sounding using FIR and submillimeter emission spectroscopy from balloons was begun by Carli and coworkers three decades ago [2–6]. Application of this technique in observing the atmosphere from space was pioneered by the Microwave Limb Sounder (MLS) [7] aboard NASA's Upper Atmosphere Research Satellite (UARS) which was launched in 1991. The Sub-Millimeter Radiometer (SMR) [8] aboard the Odin satellite was launched in 2001 and provides global information on ozone and species of importance for ozone chemistry by detecting limb thermal emissions in the spectral range of 486–581 GHz as well as one millimeter-wave band at 119 GHz. In 2004, NASA launched an advanced successor to the previous MLS, the Earth Observing System (EOS) MLS [9] on board the Aura satellite, which measures many chemical species with better global and temporal coverage and resolution. The Superconducting subMIllimeter-wave Limb-Emission Sounder (SMILES) [10], a joint spaceborne mission of the Japan Aerospace Exploration Agency (JAXA) and the National Institute of Information and Communications Technology (NICT), was attached to the Japanese Experiment Module (JEM) on the International Space Station (ISS) and delivered atmospheric observations from 12 October 2009 to 21 April 2010.

Spaceborne limb emission spectroscopy has the advantage of providing continuous global-scale observations, allowing for the inference of long-term trends in atmospheric concentrations and temperature profiles. However, to meet unique scientific needs with highly reliable and stable technology, space-based missions are always expensive and have a long development period. Owing to lower costs during the launch and operating phases, limb-sounding instruments operated on stratospheric balloon gondolas are a good alternative for mapping vertical distributions of reactive and reservoir species that can be used to address chemical processes in the middle atmosphere. Although a balloon can only be operated on a local scale within a short period of time (ideally up to 2–3 days), balloon-borne observations with high sensitivity and flexible sampling density can provide scientific experience for data acquisition and evaluation. In addition to the above-mentioned works by Carli's group, the balloon-borne FIR Spectrometer (FIRS-2) [11] has been flown many times to perform measurements of stratospheric minor species [12–15]. Besides, balloon campaigns have been proven to be valuable for the validation of spaceborne missions. Measurements of atmospheric tracers recorded by MIPAS-B [16], the balloon version of the Michelson Interferometer for Passive Atmospheric Sounding (MIPAS) [17] throughout the thermal infrared (TIR) region, have been used for validating the sensors on the ESA's Envisat satellite [18–23], the Japanese Improved Limb Atmospheric Spectrometer (ILAS)/ILAS-II satellite sensor [24], and the SMILES instrument on the ISS [25]. Likewise, the Limb Profile Monitor of the Atmosphere (LPMA) [26] operated by the Laboratoire de Physique Moleculaire et Applications at the French National Center for Scientific Research (CNRS) has been used to validate satellite instruments onboard the Envisat. Additionally, balloon-borne sensors have served as precursors to future spaceborne instruments, e.g., BSMILES [27], and BMLS [28], etc. Last but not least, balloon-borne instrument prototypes can serve as test beds for new solutions to potential technical difficulties in the design of new instruments.

The TErahertz and submillimeter LImb Sounder (TELIS) [29], cooperatively developed by the German Aerospace Center (DLR), the Netherlands Institute for Space Research (SRON), and the Rutherford Appleton Laboratory (RAL) in the UK, is a cryogenic multi-channel heterodyne spectrometer designed to study atmospheric chemistry and dynamics, with a focus on the stratosphere. TELIS is a compact, lightweight instrument capable of providing broad spectral coverage, high spectral resolution, and extensive flight duration. The TELIS instrument obtains FIR and submillimeter measurements simultaneously by carrying a tunable 1.8-THz channel [30] and a tunable 480–650 GHz

channel [31], respectively. The instrument was designed to be installed on a balloon platform together with MIPAS-B from the Karlsruhe Institute of Technology (KIT). This new combination of sophisticated sensors yields an extended spectral range for investigating atmospheric chemistry in the upper troposphere and stratosphere and offers large synergies for cross-validating measured common gas species. Pre-launch/laboratory characterization campaigns revealed that TELIS can observe the atmosphere with a vertical resolution of $\sim$2 km below the balloon float altitude [29]. After a test flight in 2008 in Teresina, Brazil, the TELIS instrument participated in three scientific campaigns on 11 March 2009, 24 January 2010, and 31 March 2011, respectively. The balloon was launched from Kiruna, Sweden and landed after about 12–14 h. These three winter flights are particularly important for validating coincident spaceborne observations, for instance TELIS for SMILES/JEM and MLS/Aura [25,32], and MIPAS-B for MIPAS/Envisat [33]. The latest joint balloon campaign took place on 7 September 2014 over Ontario, Canada.

Detailed information about the sensor design and the measurement capabilities of the TELIS 480–650 GHz channel can be found in [31,34–37]. A feasibility study of isotopic water retrievals using synthetic TELIS data and the first results of hydrogen chloride (HCl) and chlorine monoxide (ClO) using real data during the 2010 campaign were presented in [38,39], respectively. However, radiometric applications using 1.8-THz signals have been rarely exploited for atmospheric research, although there are a number of studies using FIR spectroscopy, for example the 2.5-THz signals measured by the MLS/Aura [40] and the Terahertz OH Measurement Airborne Sounder (THOMAS) [41], the 3.5-THz hydroxyl radical (OH) signature used by a balloon-borne FIR Fourier transform spectrometer [5,42], combined 3.0- and 3.5-THz signals observed by the Far-Infrared Limb Observing Spectrometer (FILOS) [43], and the 11 OH rotational transitions over 2.5–6.9 THz detected by FIRS-2 [15]. To the best of our knowledge, 1.8-THz radiation has not been utilized for atmospheric profiling.

The stratosphere over the northern polar region has exerted a lot of attraction, as the ozone loss in Arctic winters shows a fairly complex correlation with temperature variations and stratospheric chemistry/dynamics [44] in the wintertime polar vortex [45]. Satellite limb sounders were used to monitor the ozone loss during the 2009/2010/2011 Arctic winters, e.g., [46,47]. Several airborne campaigns observing the Arctic atmosphere were carried out in Kiruna and the corresponding measurements were analyzed in [48,49]. Likewise, the primary scientific objective of the three TELIS/MIPAS-B winter flights over the period 2009–2011 was to measure vertical distributions of atmospheric species that affect stratospheric ozone depletion. Chlorine activation occurs in the stratosphere during the polar winter, when the sun does not rise over the polar region so that atmospheric temperatures are extremely low and PSCs are formed [50]. Hydrogen chloride (HCl) is the main chlorine reservoir species monitored by both channels of TELIS, whereas the active chlorine species chlorine monoxide (ClO) is only observed by the 480–650 GHz channel. These species have been used for a quantitative estimation of the total budget of chlorine in the stratosphere and allow a better understanding of their impact on stratospheric ozone depletion [51,52]. Carbon monoxide (CO) is a tracer related to atmospheric transport as a result of its long lifetime in the atmosphere. Winter polar descent in the vortex brings CO-rich air downward into the stratosphere [53]. Moreover, CO is an ideal tracer of vortex dynamics until springtime, since there is little OH in the stratosphere and lower mesosphere to destroy CO during the polar night of the wintertime. Remote sensing of OH is rather appealing, because OH is an important reactive tracer that affects ozone and provides observational evidence of OH response to solar radiation. The capabilities for deriving information on vertical profiles of stratospheric species from FIR limb emission measurements in the northern polar region should be assessed. Moreover, a better understanding of the TELIS instrument performance and measurement characteristics should be achieved.

This work analyzes data from the TELIS 1.8 THz channel and aims to investigate the quality of retrieved profiles. For the first time, we present concentration profiles of stratospheric trace gases retrieved from the FIR measurements of TELIS during the three winter campaigns in 2009, 2010,

and 2011, respectively. An overview of the instrument and measurement concepts of the 1.8 THz channel is given in Section 2. The retrieval framework comprising the forward module and the inversion algorithm is briefly described in Section 3. In Section 4, the quality of retrieved O_3, HCl, CO, and OH profiles is discussed in terms of the inversion accuracy, goodness of fit, and the exploitation of information content from the measurement that are characterized by the total retrieval error, the residual, and the averaging kernel, respectively. An extensive error characterization, including the quantification of smoothing, noise, and (forward and instrument) model parameters errors is presented. In addition, these profiles (except for OH) are compared with the products obtained by the TELIS 480–650 GHz channel and MIPAS-B, as well as spaceborne limb sounders, i.e., SMILES/JEM, MLS/Aura, and SMR/Odin (hereafter SMILES, MLS, and SMR). Finally, Section 5 summarizes the main lessons learned from this work and discusses the implications for future studies.

2. Overview of TELIS Measurements

2.1. Instrument

The TELIS instrument utilizes state-of-the-art superconducting heterodyne technology and both 1.8 THz and 480–650 GHz channels operate simultaneously. The incoming atmospheric signals are transmitted from a dual offset Cassegrain telescope through the front-end transfer optics where the signals are separated and coupled into dedicated channels. At the TELIS backend, a digital autocorrelator spectrometer with a spectral resolution of 2.16 MHz is used to yield the digitized autocorrelation of the measured signal as raw data, i.e., the Level-0 (L0) data product. The signals of the THz/GHz channels are then split into four frequency segments with 500-MHz bandwidth and converted into the power spectra by the Fourier transform of the true autocorrelation function [29,31,35].

The TELIS L0 data is post-processed on ground to obtain Level-1b (L1b) data products. The TELIS L1b data product consists of radiometrically and spectrally calibrated radiance spectra along with relevant geolocation data and tangent height information. Besides, a set of instrumental parameters including information of sideband ratios (r) and antenna beam profiles is given. The average system noise temperature T_{sys} ranges between 3000 and 4000 K in the case of the 1.8-THz channel [29].

The TELIS 1.8-THz channel measures the atmospheric signal between 1790 GHz and 1880 GHz, applying a tunable local oscillator (LO). For each measurement, almost $\sim$1000 frequency points are distributed over the 2-GHz intermediate frequency (IF) bandwidth (f_{IF} ranges from 4 to 6 GHz), i.e., the spectrum I is the weighted superposition of the spectra of the two sidebands:

$$I = \frac{r}{r+1} I_{\mathrm{USB}} + \frac{1}{r+1} I_{\mathrm{LSB}}\,, \tag{1}$$

where I_{USB} and I_{LSB} denote the spectra of the upper and lower sidebands ($f_{\mathrm{LO}} + f_{\mathrm{IF}}$ and $f_{\mathrm{LO}} - f_{\mathrm{IF}}$), respectively.

The TELIS measurements are performed using a set of narrow (2-GHz width) spectral intervals called "microwindows". The main selection criterion of a proper microwindow is to have isolated spectral lines of the target species with insignificant overlapping contributions from other interfering species. With the chosen LO frequency, the microwindows have been measured sequentially in the same cryostat cooling cycle as the flight itself was performed [29].

Both TELIS and MIPAS-B were connected to the balloon gondola frame by springs, which may deteriorate the pointing stability. The relevant pointing information was provided by the Attitude and Heading Reference System (AHRS) [16] and its uncertainty is within 1 arcmin. It has been suggested that the pointing information can be derived from measurements of oxygen emission lines [54–58]. However, due to the very high noise temperature in the TELIS O_2 microwindow, an accurate retrieval of the pointing information is not feasible; further, it is not required because of the high quality of the AHRS data.

In addition, a linear calibration scheme was implemented for the L1b measurements, deploying the two signal references: an onboard blackbody as a hot signal reference, and the signal from pointing into deep space as a cold signal reference with a temperature of 2.725 K. In order to reduce noise and drift effects, a polynomial fit of the measured cold and hot calibration spectra has been used.

For more details on the TELIS 1.8 THz channel and its L1 data processing, see [59] (available at https://elib.suub.uni-bremen.de/edocs/00101711-1.pdf) and references therein.

2.2. Limb Spectra

A single limb-scanning sequence consists of a series of radiance spectra with equidistant steps between two consecutive tangent points. During flights, the balloon gradually lifts up and after 3–4 h reaches an altitude of about 30–40 km, where most of the spectral observations are recorded by the multi-instrument payload. Typical limb spectra measured by TELIS are characterized by tangent heights ranging from 10 or 16 km up to the highest tangent point ($\sim$ 2–3 km below the balloon float altitude) discretized in 1.5- or 2-km steps. The antenna beam profile (i.e., the azimuthally collapsed antenna response versus the vertical coordinate) defines the field-of-view (FoV) of the 1.8-THz channel and was measured via a method introduced in [40]. The measurements show no LO frequency dependency, and are stable over time. The FoV is Gaussian-shaped with a full width half maximum (FWHM) in the vertical direction of $0.1043 \pm 0.0008^{\circ}$. The tangent offset with respect to the commanded tangent height (taken from the AHRS pitch 0°) is 3.4 arcmin, indicating that the actual tangent height of a pencil beam is slightly higher than the commanded one. In this section, the TELIS spectra used for atmospheric concentration retrievals are briefly explained.

Figure 1 shows typical limb sequences corresponding to four different microwindows. O_3 features occur almost in every microwindow detected by both channels of the TELIS instrument. Consequently, the TELIS consortium did not define any dedicated ozone microwindow during these three campaigns. To choose a proper ozone line for the retrieval, one should take into account the energy of the lower state where the transition occurs since this quantity reflects the expected sensitivity to atmospheric temperature [57].

Semi-heavy water (HDO) retrievals will not be discussed in this study, and nevertheless, the HDO microwindow can be regarded as a good choice for retrieving O_3. An evident O_3 feature is distributed over the first two segments, and its peak is near the border of the two adjacent segments. A slightly weak O_3 signature can be noticed in segment 4, but is located in the wing of a strong O_3 line centered outside the detected frequency range.

TELIS probes CO at the transition frequency of 1841.36 GHz ($\sim 61.42\,\mathrm{cm}^{-1}$). The segment of 4.5–5 GHz contains a strong CO feature from the upper sideband. A pair of O_3 signatures is discernible in both wings of the CO line and is located in segments 1 and 3. Since a weak HOCl feature resides in the left wing of the CO line, HOCl needs to be retrieved for a better fit.

A distinguishable $H^{37}Cl$ signature at 1873.40 GHz ($\sim 62.49\,\mathrm{cm}^{-1}$) was observed by the TELIS instrument during the 2010 flight. In the microwindow with $f_{LO} = 1877.6323$ GHz, this HCl line is noticeable around the intermediate frequency of about 4.2 GHz (segment 1) with negligible overlapping contributions from other species (e.g., O_3 and H_2O). This HCl signal originates from the lower sideband and an abnormal dip can be seen as a result of the atmospheric spectra calibrated by the up-looking spectrum with a zenith angle of 25° instead of the cold signal reference at the temperature of 2.725 K. Therefore, this calibration process should be taken into account in the forward model, otherwise it could hamper the retrieval.

Most OH measurements taken from the 2009 flight utilized the 1834.75-GHz transition. Together with the H_2O contamination, a strong O_3 feature is found on the left-hand side of the OH feature, inducing a sloped background, particularly for the lowermost altitudes. In this regard, an accurate estimation of OH is expected to be affected by the morphology and amount of atmospheric ozone. Additionally, the discontinuities between neighboring segments caused by baseline shifts and varying spectral response can be treated by ignoring a few spectral points around the boundary.

These discontinuities are dependent on the spectral distribution within the channels together with which autocorrelator segment is used. Since the 1.8-THz channel always utilizes the same autocorrelator for different microwindows, it is not characteristic of a single autocorrelator, but of combined autocorrelators and a microwindow. It is plausible that the OH retrieval at lower altitudes is profoundly governed by the a priori knowledge.

As can be seen in Figure 1, these terahertz microwindows are mostly contaminated by significant H_2O contributions. Apparently, the treatment of H_2O profile and broadband continuum knowledge turns out to be vital to the quality of retrieved target species, and this is discussed in Section 3.2.

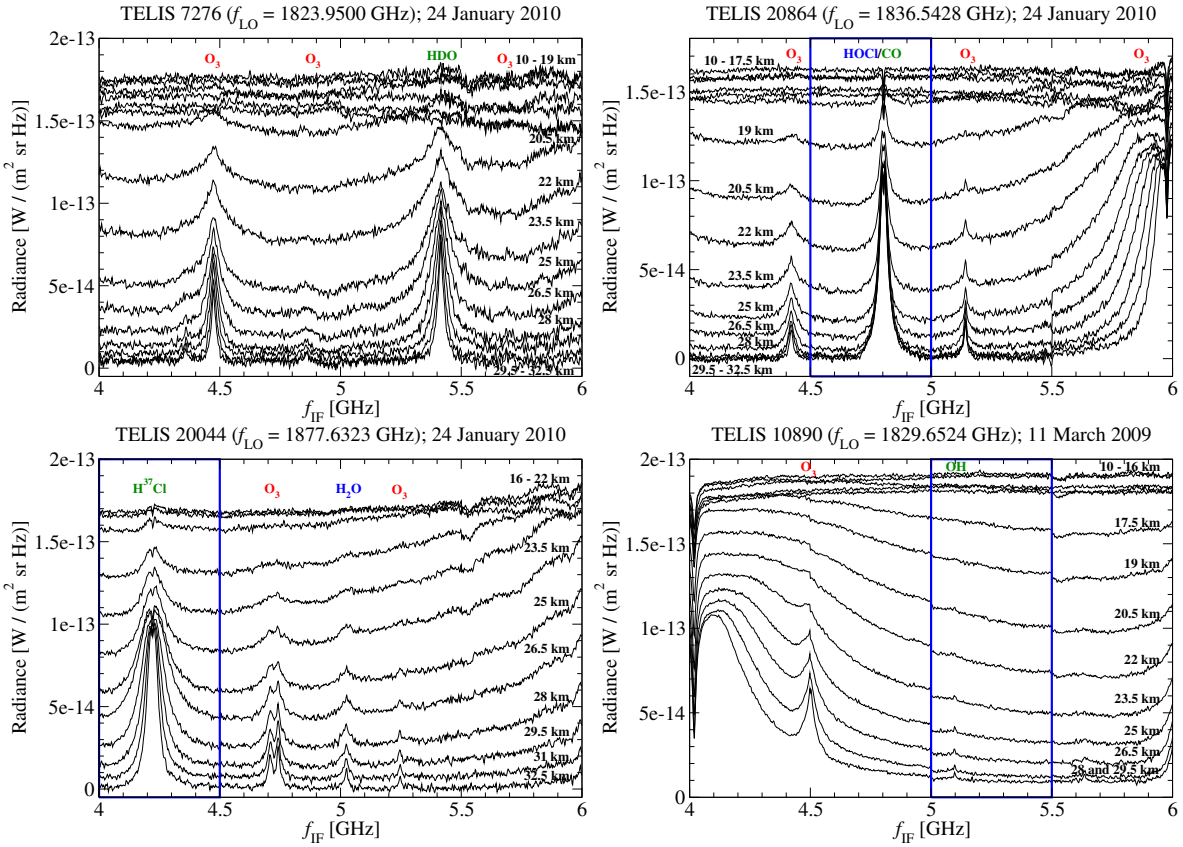

Figure 1. Typical sequences of limb spectra corresponding to four microwindows (top left: semi-heavy water (HDO), top right: carbon monoxide (CO); bottom left: hydrogen chloride (HCl), bottom right: hydroxyl radical (OH)) measured by the TErahertz and submillimeter LImb Sounder (TELIS) 1.8-THz channel during the 2009 and 2010 flights. These limb sequences, covering tangent heights from 10 or 16 km up to 32.5 km in steps of 1.5 km, are illustrated as a function of intermediate frequency f_{IF}. Please note that 7276, 20864, 20044, and 10890 are the associated measurement identifiers.

3. Retrieval Methodology

3.1. Inversion Framework

For processing the L1b spectra from the TELIS 1.8-THz channel, a retrieval algorithm known as Profile Inversion for Limb Sounding (PILS) [60,61] was developed at the DLR. It consists of two parts, a forward model built on the Generic Atmospheric Radiation Line-by-line Infrared Code (GARLIC) [62], and an inversion scheme that iteratively minimizes the differences between observed and simulated radiance spectra by adjusting atmospheric and model parameters of interest.

The goal of inversion is to retrieve the vertical concentration profiles (volume mixing ratio, VMR) comprising the state vector $\boldsymbol{x} \in \mathbb{R}^n$, while the forward model $\boldsymbol{F}$ maps the state vector $\boldsymbol{x}$ into the spectra

$\boldsymbol{y}^{\delta} \in \mathbb{R}^m$, i.e., $\boldsymbol{F} : \mathbb{R}^n \rightarrow \mathbb{R}^m$, where m is the number of spectral radiances, and n is the number of unknowns. In the framework of Tikhonov-type regularization, the inversion process seeks the minimizer of the objective function $\mathcal{F}(\boldsymbol{x})$:

$$\mathcal{F}(\boldsymbol{x}) = \|\boldsymbol{F}(\boldsymbol{x}) - \boldsymbol{y}^{\delta}\|^2 + \lambda \|\mathbf{L}(\boldsymbol{x} - \boldsymbol{x}_{\mathrm{a}})\|^2 \quad (2)$$

$$= \left\| \begin{array}{c} \boldsymbol{F}(\boldsymbol{x}) - \boldsymbol{y}^{\delta} \\ \sqrt{\lambda}\mathbf{L}(\boldsymbol{x} - \boldsymbol{x}_{\mathrm{a}}) \end{array} \right\|^2 , \quad (3)$$

with $\mathbf{L}$, λ, and $\boldsymbol{x}_{\mathrm{a}}$ representing the regularization matrix, the regularization parameter, and the a priori profile, respectively. The inversion deals with the underlying multi-component problem of jointly retrieving several vertical concentration profiles and auxiliary parameters (e.g., baseline offset), and therefore, all individual regularization terms are assembled into a global matrix $\mathbf{L}$ [63]. The form of $\mathbf{L}$ can be an identity matrix or a discrete approximation of a derivative operator. Here, the Cholesky factor of an a priori profile covariance matrix $\mathbf{S}_{\boldsymbol{x}}$ is used:

$$\mathbf{L}^T\mathbf{L} = \mathbf{S}_x^{-1} , \quad (4)$$

where

$$[\mathbf{S}_x]_{ij} = \sigma_{xi}\sigma_{xj}[\boldsymbol{x}_{\mathrm{a}}]_i[\boldsymbol{x}_{\mathrm{a}}]_j \ \exp\left(-2\frac{|z_i - z_j|}{l_i + l_j}\right) , \quad (5)$$

σ_{xi} are the profile standard deviations, and l_i are the altitude-independent correlation lengths. In our case, l_i are chosen to be identical to the vertical spacing of two adjoint tangent points. This choice allows some freedom to deviate away from the a priori profile, while suppressing large oscillations in the non-unique solution space.

An optimization of the objective function is based on a trust-region strategy [64] and a Gauss–Newton model, which yields the next iterate:

$$\boldsymbol{x}_{\lambda,i+1} = \boldsymbol{x}_{\mathrm{a}} + \left(\mathbf{K}_i^T\mathbf{K}_i + \lambda\mathbf{L}^T\mathbf{L}\right)^{-1}\mathbf{K}_i^T\left(\boldsymbol{y}^{\delta} - \boldsymbol{F}(\boldsymbol{x}_{\lambda,i}) + \mathbf{K}_i(\boldsymbol{x}_{\lambda,i} - \boldsymbol{x}_{\mathrm{a}})\right) , \quad (6)$$

where $\mathbf{K}_i$ is the Jacobian matrix of $\boldsymbol{F}(\boldsymbol{x}_{\lambda,i})$ evaluated at $\boldsymbol{x}_{\lambda,i}$ and generated by means of automatic differentiation (AD) [65,66]. AD offers accurate derivatives for working precision and significant speed-up compared to finite difference (FD) approximations whose accuracy is subject to the amount of perturbation. An in-depth assessment of AD and FD Jacobians can be found in [67]. According to www.autodiff.org, "manual implementation of analytic derivative formulae typically produces efficient derivative code. However, the implementation can be tedious and error-prone." Currently, GARLIC and its variants (such as PILS) use the source-to-source AD tool TAPENADE [68].

The regularization parameter λ is vital to the final output of the inversion and needs to be estimated properly, such that the regularized solution $\boldsymbol{x}_{\lambda}$ is sufficiently close to the exact solution, and the model spectra with $\boldsymbol{x}_{\lambda}$ fit the measurements adequately well. However, the estimation of λ can require considerable computational effort and improper estimates of λ can deteriorate the quality of the retrieval product. In addition, the iteration should be terminated when the residual is below the noise level. However, in our case, the noise level cannot be estimated (owing to the forward model errors). Thus, we adopt the iteratively regularized Gauss–Newton method [69,70], i.e., λ in Equation (6) is gradually decreased at each iteration and termination of the iterative process is controlled by the discrepancy principle [71,72]: the stopping index i^* is after the convergence of the residuals which should be within a prescribed tolerance,

$$\left\|\boldsymbol{F}(\boldsymbol{x}_{\lambda,i^*}) - \boldsymbol{y}^{\delta}\right\|^2 \leq \chi\left\|\boldsymbol{r}^{\delta}\right\|^2 < \left\|\boldsymbol{F}(\boldsymbol{x}_{\lambda,i}) - \boldsymbol{y}^{\delta}\right\|^2 , \qquad 0 \leq i < i^* , \quad (7)$$

where $\left\|\boldsymbol{r}^{\delta}\right\|$ is the residual norm at the last iteration step, and $\chi > 1$ is a control parameter.

The inversion carried out by PILS generally converges in less than 10 iterations, depending on the regularization method used. An extensive assessment of the numerical performance of iterative and direct Tikhonov-type regularization approaches was discussed in [73], demonstrating that the iteratively regularized Gauss–Newton method can produce plausible retrieval results and largely spare the extra computation time for estimating λ.

After convergence, an error characterization of uncertainties due to smoothing ($\boldsymbol{e}_\mathrm{s}$), measurement noise ($\boldsymbol{e}_\mathrm{y}$), and instrument and forward model parameters ($\boldsymbol{e}_\mathrm{c}$ and $\boldsymbol{e}_\mathrm{b}$, respectively) is performed:

$$\boldsymbol{e}_\lambda = \boldsymbol{e}_\mathrm{s} + \boldsymbol{e}_\mathrm{y} + \boldsymbol{e}_\mathrm{c} + \boldsymbol{e}_\mathrm{b} \,. \tag{8}$$

In particular, the forward model and instrument model errors in the state space $\boldsymbol{e}_\mathrm{b}$ and $\boldsymbol{e}_\mathrm{c}$ are caused by inaccurate knowledge of the forward model parameters $\boldsymbol{b}$ (essentially atmospheric and spectroscopic parameters) and the instrument model parameters $\boldsymbol{c}$, respectively. If $\Delta\boldsymbol{b}$ are the uncertainties in $\boldsymbol{b}$, the forward model error in the state space $\boldsymbol{e}_\mathrm{b}$ is computed from the forward model error in the data space $\boldsymbol{\delta}_\mathrm{b}$ by means of

$$\boldsymbol{e}_\mathrm{b} = \mathbf{K}_\lambda^\dagger \boldsymbol{\delta}_\mathrm{b} = \mathbf{K}_\lambda^\dagger \mathbf{K}_\mathrm{b} \Delta\boldsymbol{b} \approx \mathbf{K}_\lambda^\dagger \left[\boldsymbol{F}(\boldsymbol{x}_\mathrm{t}, \boldsymbol{b} + \Delta\boldsymbol{b}) - \boldsymbol{F}(\boldsymbol{x}_\mathrm{t}, \boldsymbol{b})\right] \,, \tag{9}$$

where $\mathbf{K}_\mathrm{b}$ is the Jacobian matrix with respect to the forward model parameters, i.e., $\partial\boldsymbol{F}/\partial\boldsymbol{b}$. Likewise, the instrument model error in the state space $\boldsymbol{e}_\mathrm{c}$ can be computed from the instrument model error in the data space $\boldsymbol{\delta}_\mathrm{c}$:

$$\boldsymbol{e}_\mathrm{c} = \mathbf{K}_\lambda^\dagger \boldsymbol{\delta}_\mathrm{c} = \mathbf{K}_\lambda^\dagger \left[\boldsymbol{R}\left(\boldsymbol{s}, \boldsymbol{c} + \Delta\boldsymbol{c}\right) - \boldsymbol{R}\left(\boldsymbol{s}, \boldsymbol{c}\right)\right] \,, \tag{10}$$

where $\boldsymbol{R}$ is the instrument model function, $\boldsymbol{s}$ is the signal delivered by the instrument, and $\Delta\boldsymbol{c}$ are the uncertainties in $\boldsymbol{c}$.

Given the regularized generalized inverse $\mathbf{K}_\lambda^\dagger$ in Equations (9) and (10), the averaging kernel matrix is given by

$$\mathbf{A} = \mathbf{K}_\lambda^\dagger \mathbf{K} = \left(\mathbf{K}^T\mathbf{K} + \lambda \mathbf{L}^T\mathbf{L}\right)^{-1} \mathbf{K}^T\mathbf{K} \,. \tag{11}$$

The trace of $\mathbf{A}$ gives the degree of freedom for the signal (DOFS), the sum of the elements of each averaging kernel row yields the measurement response, and the widths of $\mathbf{A}$ can be interpreted as a measure of the vertical resolution.

It is worth mentioning that our retrieval is formulated in a semi-stochastic framework, and accordingly, the smoothing and model parameter errors are assumed to be deterministic, whereas the noise error is assumed to be stochastic with zero mean and covariance matrix $\mathbf{S}_\mathrm{y}$. In practice, the accuracy of the regularized solution can be estimated through the mean square error matrix $\mathbf{S}_\lambda$, and the sum of the square root of the diagonal elements of $\mathbf{S}_\lambda$ gives the expected value of the retrieval error:

$$\mathbf{S}_\lambda = \mathcal{E}\left\{\left(\boldsymbol{x}_\lambda - \boldsymbol{x}_\mathrm{t}\right)\left(\boldsymbol{x}_\lambda - \boldsymbol{x}_\mathrm{t}\right)^T\right\} \approx \mathbf{S}_\mathrm{s} + \mathbf{S}_\mathrm{y} + \mathbf{S}_\mathrm{b} + \mathbf{S}_\mathrm{c} = \boldsymbol{e}_\mathrm{s}\boldsymbol{e}_\mathrm{s}^T + \sigma^2 \mathbf{K}_\lambda^\dagger \mathbf{K}_\lambda^{\dagger T} + \boldsymbol{e}_\mathrm{b}\boldsymbol{e}_\mathrm{b}^T + \boldsymbol{e}_\mathrm{c}\boldsymbol{e}_\mathrm{c}^T \tag{12}$$

with $\mathcal{E}$ representing the expected value operator. The total retrieval error $\boldsymbol{e}_\lambda$ is defined as the root sum squares (RSSs) of all these above-mentioned error components in Equation (12), rather than treating them as a direct sum in Equation (8).

For more details on the theoretical aspects of the forward module and inversion algorithm, we refer to [60–62].

3.2. Retrieval Setup

The TELIS retrievals were conducted on an altitude grid with an equidistant vertical spacing identical to the tangent height step of the limb sequence (1.5 or 2 km) below the float altitude of

the balloon gondola. The bottom level of the retrieval grid was set below the lowest tangent point by 1.5 km due to the extended vertical FoV of the instrument and the pointing uncertainty. Here, the top-of-atmosphere was set to 65 km for two reasons: First, the atmosphere above TELIS may be crucial to the molecules with weak spectral signatures, such as HCl and OH. Second, a sufficient length of the state vector needs to be ensured so as to reach a best compromise between computational efficiency and inversion quality. In this regard, the state vector $\boldsymbol{x}$ comprises the VMR profiles over 8.5–65 km or 14.5–65 km.

Accurate forward model parameters are always a key to a reliable retrieval product. Here, the a priori temperature and pressure profiles were taken from the MIPAS-B retrievals and the European Center for Medium-range Weather Forecasts (ECMWF) data, respectively. The associated error in the temperature profile was expected to be lower than $\sim$1 K [74]. The retrieved TELIS O_3 profile was used as the a priori information for estimating other species. In the case of strong water vapor contamination, the H_2O profile was jointly retrieved to improve the fit. The profiles of interfering gas species that are of minor importance were fixed to the Air Force Geophysics Laboratory (AFGL) subarctic winter atmosphere [75]. The semi-empirical Clough–Kneizys–Davis (CKD) [76] model was adopted to account for broadband continuum contributions. For our retrieval, a precise knowledge of the continuum is not required because a empirical "continuum" and "greybody" were fitted along with the "main" unknowns (discussed in the next paragraph). All relevant spectroscopic parameters were extracted from the HIgh-resolution TRANsmission (HITRAN) 2012 database [77]. For completeness, Table 1 summarizes the a priori profiles, the discretization scheme, and other forward model parameters used in this analysis.

Table 1. Retrieval configurations for the reconstruction of atmospheric vertical concentration profiles from the TELIS limb spectra in the far infrared (FIR) region. The settings for the chosen retrieval grid, atmospheric inputs, and other forward model parameters are listed. MIPAS-B: Michelson Interferometer for Passive Atmospheric Sounding–Balloon; ECMWF: European Center for Medium-range Weather Forecasts; AFGL: Air Force Geophysics Laboratory; CKD: Clough–Kneizys–Davis; HITRAN: HIgh-resolution TRANsmission.

Retrieval Configuration	Description
Discretization	
Bottom-of-atmosphere	8.5 or 14.5 km
Top-of-atmosphere	65 km
8.5–32.5 km (14.5–32.5 km)	1.5 or 2 km
32.5–40 km	2.5 km
40–65 km	5 km
Temperature profile	MIPAS-B retrievals
Pressure profile	ECMWF
Remaining interfering species	AFGL subarctic winter model
Water vapor continuum	CKD model
Spectroscopic line parameters	HITRAN 2012

The limb spectral baseline in the infrared and microwave range is strongly affected by contributions having continuum-like behavior, and these continuum-like contributions are possibly due to broad spectral features of trace gases, effects associated with spectral line shape, and aerosols and cirrus cloud particles in the upper troposphere and lower stratosphere [78]. Many studies (e.g., [48,79–81]) suggest that this can be achieved by the joint-fitting of an additional artificial molecule termed the "greybody" in order to simulate the continuum-like absorption at each altitude level, which is particularly necessary for lower altitude levels where these broad continuum signatures are not sufficiently represented by current continuum models. An example given in [62] demonstrated the importance of this approach used in the TELIS retrieval, removing the large discrepancies over the strong lines at the lower tangent altitudes and ultimately resulting in substantially reduced residuals.

Thus, to fully characterize the continuum effects, our retrieval approach uses the "greybody" fitting together with the CKD model.

In addition to concentration profiles of the target molecule(s), a constant baseline was retrieved for each spectrum with the aim of compensating the instrumental effects (e.g., imperfect calibration processes, self-emission of the instrument). Radiometric accuracy is very important for well-qualified profile retrieval. In particular, systematic radiometric errors can lead to a shift in the retrieval. The radiometric calibration process has been modeled in the PILS algorithm and the corresponding mathematical expressions were given in [60].

With the exception of O_3, the retrievals were performed by using a single frequency segment (500 MHz) instead of the whole microwindow (2 GHz). Exploiting a single segment allows a better spectral baseline fit and reduces the number of interfering molecules; furthermore, problems due to the discontinuities across the segment bounds are avoided.

3.3. Error Characterization

In this study, the most important model parameter error sources defined by the TELIS consortium (also consistent with previous studies, e.g., [38,39,82–84]) are taken into account. In Table 2, these error sources and their corresponding perturbation amounts are summarized.

Table 2. Model parameter errors considered in the TELIS FIR retrievals. For each error, the corresponding perturbation amount is indicated in the right column. See the text for a detailed explanation of each error source.

Model Parameter Error	Perturbation
Spectroscopic parameters	
Line strength (S)	1% (O_3) 2% (HCl) 1% (CO) 1% (OH)
Air broadening (γ_{air})	5%
Temperature dependence (n_{air})	10%
Radiometric calibration [1]	5%
Sideband ratio	0.05
Pointing information	
Systematic bias	3.4 arcmin
Uncertainty in the systematic bias	1 arcmin
Atmospheric parameters	
Temperature	1 K
Pressure	1%

[1] (Here, we consider the nonlinearity effect as the sole error source in the radiometric calibration and the value stands for the assumed compression in the measurement of the emission from a hot load.)

The impact of inaccurate spectroscopic knowledge is surveyed in terms of the line strength (S) and air broadening parameters (the air-broadened half width γ_{air} and the coefficient of temperature dependence n_{air}). As the HITRAN database does not report the uncertainty of the line strength for all O_3 lines considered in Section 4.1, the 1% perturbation in Table 2 was selected as a conservative estimate of the actual uncertainty. In the frame of the ESA-funded study "Scientific Exploitation of Operational Missions–Improved Atmospheric Spectroscopy Databases", an error in the HITRAN pure rotational line intensities was discovered: All line intensities in HITRAN were scaled by a factor of 1.04, although this factor should have been applied to the fundamentals and associated hot bands only (Iouli E. Gordon, private communication 2017). Furthermore, new TIR measurements within the above-mentioned ESA study reveal that ν_1 and ν_3 line intensities in the HITRAN database are 2% smaller. Another common issue is ozone contamination, and thus, air-broadening parameters for O_3 lines should also be considered. In the case of HCl, a line strength uncertainty of 2% was taken,

which is consistent with the one used in [39]. This perturbation amount can be seen as a conservative estimate, since these values are very well determined from electric dipole moments.

According to Buehler et al. [85], a possible pressure shift can also have an influence on the retrieval (particularly for HCl). Its impact was investigated by a systematic analysis described in [60], revealing that a perturbation of the corresponding parameter (air pressure-induced line shift) did not lead to any considerable difference in the HCl retrieval. Accordingly, the subject of pressure shift will not be discussed here.

Uncertainties in the instrument parameters for the TELIS 1.8 THz channel have been examined in past laboratory campaigns by the instrument team. Although nonlinearities present in the calibration chain have been substantially corrected in the latest L1b data product, an uncertainty of 5% was used as a conservative estimate of the compression in the hot load measurement related to the calibrated output. The sideband ratio typically ranges from 0.95 to 1.05, and in this study, an uncertainty of 5% was considered. Regarding the pointing accuracy, the systematic bias was estimated to be 3.4 arcmin in the commanded zenith angle based on the antenna beam profile measurements. An additional 1 arcmin was superimposed onto this systematic pointing bias according to the accuracy of the AHRS system. These instrument error sources have been analyzed in extensive laboratory campaigns within the frame of the PhD thesis by Peter Vogt [86].

Possible errors introduced by atmospheric inputs used in the forward model (i.e., temperature and pressure) should be assessed as well. An upper limit of 1 K was taken as the uncertainty in the MIPAS-B temperature profile, and the accuracy in the ECMWF pressure profile was estimated to be 1%.

The intrinsic property of our retrieval scheme ensures that the regularization strength is decreased iteratively in order to allow for a better altitude resolution with the drawback of slightly noisier profiles. The smoothing error is expected to be much smaller than the model parameter error in the stratosphere, whereas the noise error may be critical in some FIR microwindows where the in-flight system noise temperature was observed to be particularly high. Furthermore, the remaining nonlinearity effect of the instrument can be a major contribution to the model parameter error, especially at altitudes where the atmospheric abundances of our target molecules are high.

3.4. Comparison Strategy

The internal and external comparisons enable us to analyze the differences in the retrieval algorithms and measurement characteristics of different instruments. All observations for the comparisons were obtained by instruments that detect thermal emissions in a limb-viewing geometry. Due to a shorter flight duration of the balloon-borne instrument, the comparison with spaceborne observations can be only done on a daily basis.

The MIPAS-B instrument mounted on the same balloon with TELIS has been used to validate ozone measured by satellite instruments [24,87,88]. The corresponding retrieval algorithm is built upon the Karlsruhe Optimized and Precise Radiative transfer Algorithm (KOPRA, [80]) and a Tikhonov-type regularization approach. The vertical resolution of the MIPAS-B ozone retrieval is of 2–3 km up to the balloon height. The noise error is no more than 1%, whereas the retrieval error including systematic effects (mainly spectroscopy) reaches roughly 8–10%. More information about the MIPAS-B retrieval scheme is detailed in [52] and references therein.

The first results of HCl derived from the TELIS 480–650 GHz channel data have been presented and validated against the MLS data [39], showing that the differences between these two profiles fall well within the assumed uncertainties. The retrieval algorithm used by de Lange et al. [39] employs a Gauss–Newton scheme constrained by Tikhonov regularization. Up to the balloon height, the retrieval accuracy for the TELIS 480–650 GHz channel is within 0.5 ppbv and the vertical resolution is about 2–4 km. This also gives us an opportunity to include the profiles derived from the 480–650 GHz channel data into our internal comparison.

The SMILES profiles for the comparison were taken from the NICT Level-2 (L2) data products (v3.0.0, available at https://data.smiles.nict.go.jp/products/). This latest version of the L2 products

was generated using the newly calibrated L1b spectra (version 008, [89]). The corresponding data processing algorithms were described in [82]. Although the operation period of the SMILES instrument was shorter than expected due to the failure of the submillimeter local oscillator, the retrieval products of ozone and chlorine species have been validated against other ozonesonde, satellite, and balloon observations [32,90]. During the TELIS/MIPAS-B 2010 flight, SMILES was still active and its ozone observations are available for our comparisons. The error analysis in [32] shows that in the stratosphere, the retrieval error is dominated by systematic effects ($\sim$ 3–8%), with a vertical resolution of 3–6 km.

The MLS instrument takes measurements of atmospheric composition that can be used to track the stability of the stratospheric ozone layer. The corresponding L2 data products were processed by the Jet Propulsion Laboratory (JPL) and can be downloaded from https://mls.jpl.nasa.gov/index-eos-mls.php. The corresponding retrieval algorithms are described in [91]. Validations of ozone, HCl, and CO were presented in [92–96]. The total retrieval error of the MLS O_3 product is estimated to be 10–15% from the uppermost troposphere to the stratosphere, with a vertical resolution of $\sim$ 2.5 km. The total retrieval error for the HCl stratospheric product is 0.25–0.5 ppbv, with a vertical resolution of $\sim$ 3 km. Regarding CO, the vertical resolution is in the range 3.5–5 km for most of the stratosphere. The contributions from the noise and smoothing errors reach up to 0.02 ppmv and the retrieval error due to systematic effects is about 10–30%.

The SMR ozone profiles involved in our comparison were taken from http://odin.rss.chalmers.se/level2 and processed by the Chalmers University of Technology, Sweden. The expected noise error is 0.25–0.75 ppmv in the stratosphere and the systematic effects contribute to an error of up to 0.75 ppmv, with a vertical resolution of 3.5–4 km [83,97].

Pairs of coincident observations between TELIS and other instruments were selected under criteria that should be stringent enough to confirm that the same air masses can be observed, particularly for polar cases. A distance between observation geolocations within 300 km and a difference in the solar zenith angle within 3° were considered. A 1-h threshold for the time difference was applied. Furthermore, for each spaceborne instrument, we selected data that satisfied the following quality conditions:

- SMILES: O_3 profiles with measurement responses of no less than 0.8 and goodness of fit values of no more than 0.8 were used [32].
- MLS: O_3 profiles with "Quality" fields greater than 0.6 and "Convergence" fields less than 0.8 [94], as well as HCl profiles with "Quality" fields greater than 1.2 and "Convergence" fields less than 1.05 [95], and CO profiles with "Quality" fields greater than 0.2 and "Convergence" fields less than 1.4 were used [93].
- SMR: O_3 profiles with measurement responses greater than 0.75 and "QUALITY" flags equaling zero were used [83].

For the purpose of the comparison, all profiles were represented on a uniform vertical grid that was fine enough. If retrieval is carried out on a coarse grid, then an interpolation should be used. For the intercomparison between MIPAS-B and TELIS, the profiles were interpolated onto the MIPAS-B vertical grid; otherwise, the coincident profiles from spaceborne instruments were represented onto the TELIS vertical grid.

If the corresponding averaging kernels are evidently different, it can be misleading to directly compare the profiles retrieved from two different instruments. To account for the discrepancies in the measurement characteristics of these different observing systems, the comparison can be done by incorporating their averaging kernels and a priori information [98–100]. One can convolve the original high-resolution profile $\boldsymbol{x}_{\text{high}}$ with the averaging kernel matrix $\mathbf{A}_{\text{low}}$ of the instrument with lower vertical resolution. The smoothed profile is then given by

$$\boldsymbol{x}_{\text{smooth}} = \mathbf{A}_{\text{low}} \boldsymbol{x}_{\text{high}} + (\mathbf{I}_n - \mathbf{A}_{\text{low}})\, \boldsymbol{x}_{\text{a}} \,, \tag{13}$$

where $\boldsymbol{x}_{\text{a}}$ is the a priori profile used in the retrieval of the data of the lower resolution instrument.

When the coincident profiles from the other instruments have comparable vertical resolutions and vertical grids with those of TELIS, a direct comparison can be applied.

4. Results and Discussion

In this section, we present retrievals of O_3, HCl, CO, and OH from the Kiruna campaigns between 2009 and 2011. For each trace species, the corresponding diagnostic quantifiers are discussed in terms of the total retrieval error, the residual, and the averaging kernel.

4.1. O_3 Retrieval

As mentioned previously, O_3 can be estimated from any frequency segment of the TELIS instrument, but a favorable choice for retrieval should take into account the quantity of the lower state energy (E_i). The strong lines of O_3 are rotational transitions within the vibrational ground state and have low lower state energy with little temperature dependence on the line intensities. Table 3 lists the significant O_3 lines residing in the CO and HDO microwindows (see also Figure 1). When O_3 features from both sidebands are considered, an error in the sideband ratio is "averaged out" so that its influence on the retrieval can be reduced. From this perspective, a combination of frequency segments may be beneficial to the retrieval.

Table 3. Various ozone lines corresponding to the three selected FIR microwindows. Only the most significant ozone transitions are listed. Information about the sideband and segment where the O_3 line lies is given. E_i represents the energy of the lower state for the O_3 transition. LSB and USB stand for the lower and upper sidebands, respectively. The associated line parameters (position of line center and E_i) are extracted from the HITRAN database.

Position (cm^{-1})	Microwindow	Sideband	Segment(s)	E_i (cm^{-1})
60.6502	HDO	LSB	4	1383.2810
60.9857	HDO	USB	1	828.9916
60.9895	HDO	USB	1–2	183.4307
61.0067	HDO	USB	2	1990.1950
61.0300	HDO	USB	4	1370.5580
61.1129	CO	LSB	1	286.8056
61.4391	CO	USB	3	1196.0930
61.4598	CO	USB	4	364.7143

In the case of the HDO microwindow (measurement 7276), combined segments 1–2 were used to retrieve O_3, while for the CO microwindow (measurement 20864), segment 1 was taken. Figure 2 shows the averaging kernels, and the corresponding DOFS is greater than 10 in both cases. For both microwindows, the kernels peaked between 16 and 31 km and the vertical resolution above 22 km is close to the spacing of two consecutive tangent points ($\sim$ 1.5 km). The measurement response decreases dramatically with increasing altitudes above 32.5 km, revealing little information on ozone above the balloon height. The kernels broaden out at lower altitudes, indicating a lower retrieval sensitivity, which is possibly due to atmospheric attenuation by water vapor absorption and the lower amount of ozone at these altitudes.

Individual estimates of various errors for the O_3 retrieval from the CO and HDO microwindows are shown in Figure 3. As both microwindows cover different O_3 transitions, the differences are expected to impact on the corresponding retrieval error. The total error in the HDO microwindow at higher altitudes (above 25 km) is greatly contributed to by the calibration (due to nonlinearities in the IF-signal chain) and spectroscopic errors. At lower altitudes, the uncertainties in the pointing accuracy and sideband ratio are important to the total error. However, in the CO microwindow, the noise error dominates the total error above 20 km as the system noise temperature is very high, while the pointing error appears to have a leading role in determining the retrieval quality below 20 km. Another reason for exhibiting such high noise error is the use of a weaker regularization in this retrieval

so that a decreased smoothing error is obtained. As can be noticed from Figure 3, the spectroscopic accuracy is the second largest error source in the HDO microwindow but is of minor importance in the CO microwindow. One explanation for this striking difference between the two microwindows may be that the spectroscopy error increases with the O_3 line strength and a stronger O_3 spectral line is found in the HDO microwindow. The other error contributors such as the uncertainties in the radiometric calibration and in the sideband ratio are also likely to be determined by spectral line strengths, and thus by ozone concentrations.

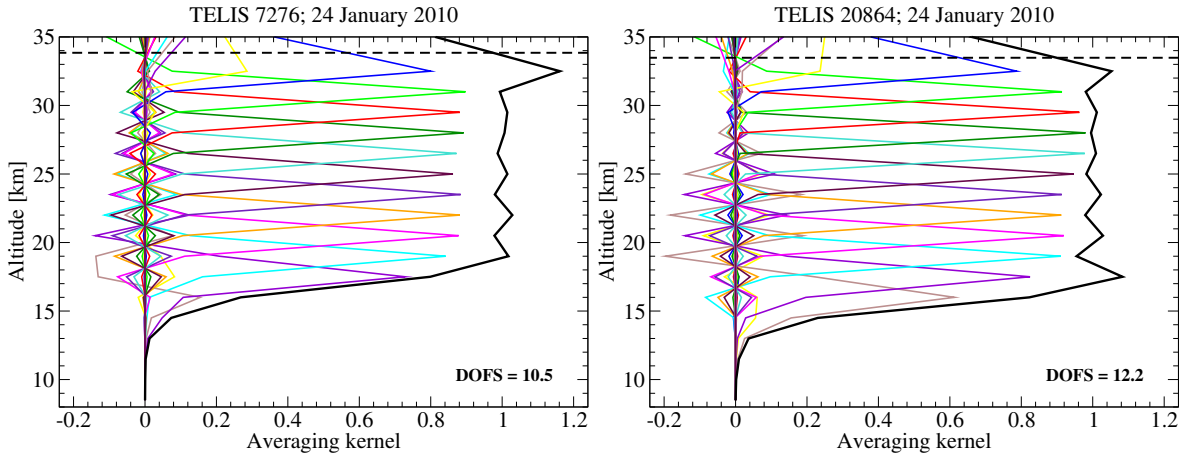

Figure 2. Averaging kernels and degree of freedom for the signal (DOFS) for the O_3 retrievals from TELIS FIR measurements, with identifiers of 7276 and 20864, respectively. Hereafter, the horizontal dashed line indicates the corresponding balloon height, and the solid black line refers to the measurement response obtained by the sum of the elements of each averaging kernel row.

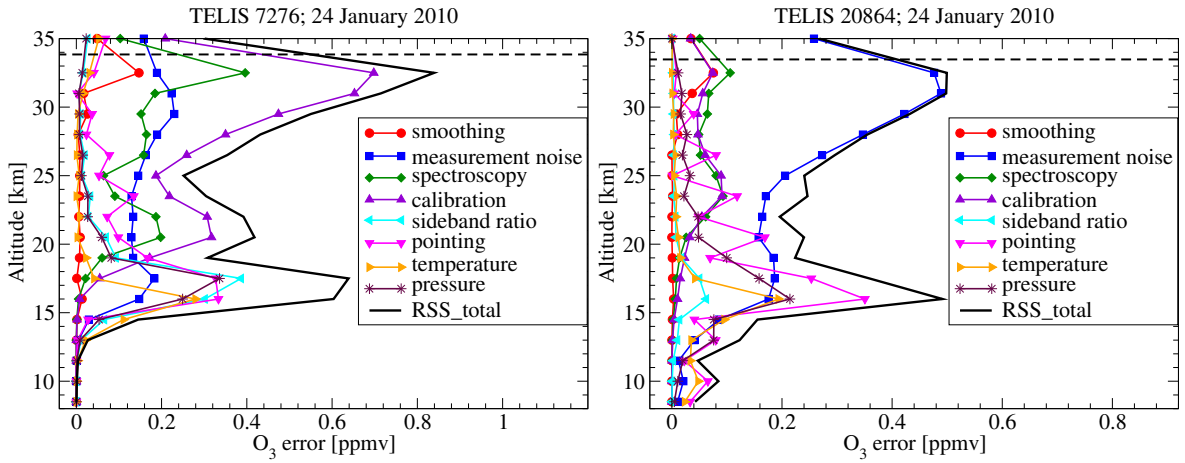

Figure 3. Individual estimates of smoothing, noise, and model parameters errors for O_3 retrieval. The estimated errors correspond to TELIS FIR measurements 7276 (HDO microwindow) and 20864 (CO microwindow) during the 2010 flight. Assumed uncertainties in the model parameter errors can be found in Table 2. The solid black line (RSS_total) refers to the total error represented by the RSS of all error components (see Equation (12)).

We first compared the TELIS retrieval with the MIPAS-B retrieval in order to ensure the consistency between both instruments on the same platform. The differences of the O_3 VMR retrieved from the two sensors are plotted in Figure 4. The altitude range where the MIPAS-B measurements have sensitivity to the gas concentrations is from the bottom of the plot ($\sim$ 8 km) to the balloon height. The comparison for the 2010 campaign (left panel of Figure 4) displays large differences between both observations over

the lower atmosphere between 09:00 h UTC and 10:00 h UTC, owing to the fact the MIPAS-B retrieval generates negative concentrations and the TELIS retrieval is affected by the a priori information. Possible reasons can be different regularization schemes used in both retrievals or subtle inadequacies in the forward model. For the 2011 campaign (right panel of Figure 4), these large discrepancies in the upper troposphere are notably reduced. In both flights, the differences increase above the balloon height where limited profile information can be inferred from the measurement. The MIPAS-B retrieval above the balloon height used different a priori setup, leading to positive and negative differences, respectively. The TELIS and MIPAS-B O_3 profiles agree very well in most of the stratosphere (between 15 and 30 km), and the TELIS profiles are slightly overestimated ($\sim$7.2% and $\sim$5.3% for 2010 and 2011, respectively) which is consistent with the bias in the ozone line strengths between the FIR and TIR regimes (see Section 3.3).

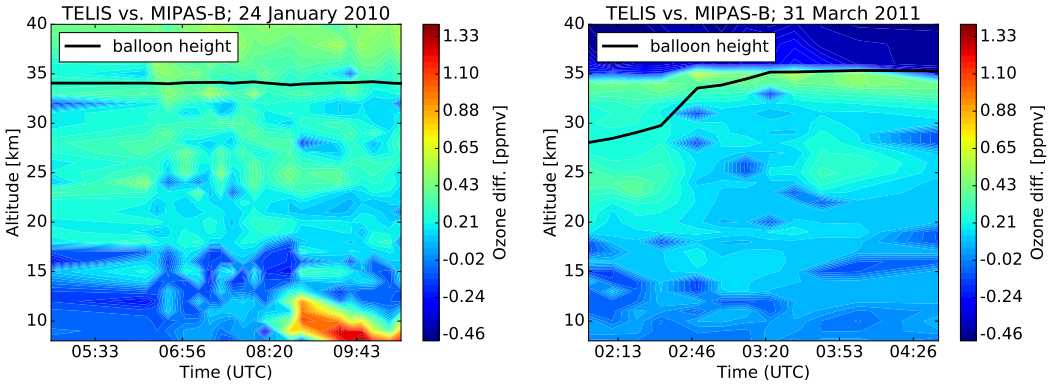

Figure 4. Difference between TELIS and MIPAS-B retrieved O_3 volume mixing ratio (VMR) profiles (TELIS − MIPAS-B) observed on 24 January 2010 and 31 March 2011. Note that both comparisons are plotted with the same difference range. Here, the balloon height is indicated by a solid black line.

MLS and SMILES probed O_3 from 240-GHz and 625-GHz measurements, respectively. A first comparison between SMILES, TELIS, and other spaceborne instruments was discussed in [32]. Figure 5 compares two TELIS O_3 profiles against three coincident spaceborne data products. For SMILES, two profiles (ID: 760, 761) were selected and the corresponding vertical resolution is 3.0–5.2 km below 35 km. Kasai et al. [32] stated that the noise and the smoothing errors of the SMILES O_3 profile are smaller than 1% of the retrieved VMR in the stratosphere. Both SMILES profiles fall well within the accuracy bounds of the TELIS profile and reach an agreement above 16 km. The MLS profile shows a similar pattern to the TELIS and has higher values between 25 and 30 km.

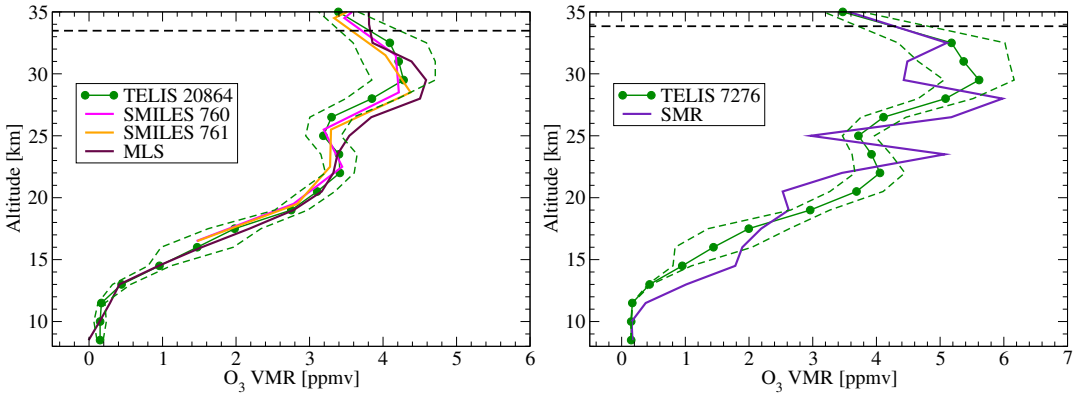

Figure 5. Comparison of O_3 profiles retrieved from TELIS, Superconducting subMIllimeter-wave Limb-Emission Sounder (SMILES), Microwave Limb Sounder (MLS), and Sub-Millimeter Radiometer (SMR) data measured on 24 January 2010. The lowest tangent height of the TELIS instrument is 10 km and the retrieval results below this altitude have little physical meaning. The dashed green lines refer to the overall accuracy of the TELIS profile. The measuring time difference of all plotted profiles was within 0.5 h. The solar zenith angles of the MLS and TELIS data were 84.0° and 85.8°, respectively.

Two coincident SMR profiles chosen for this comparison were averaged out and interpolated onto the TELIS altitude grid for a smoother profile. The SMR retrieval seems physically less valid where the measurement response is less than 0.6. Furthermore, the SMR retrieval used for this comparison appears to be underregularized, and the resulting profile oscillates around the TELIS profile.

4.2. HCl Retrieval

HCl is an important stratospheric species defined by the TELIS consortium, as both the 1.8-THz and 480–650 GHz channels observed its vertical distribution. As can be seen from Figure 1, there is a dip around the line center of HCl resulting from the in-flight radiometric calibration procedure. In this case, the cold reference spectrum in the forward model should be replaced by an up-looking spectrum with a zenith angle of 25°, which accounts for this unphysical effect. On 24 January 2010, the TELIS/MIPAS-B joint flight took place over northern Scandinavia inside the activated Arctic vortex, giving the opportunity to observe chlorine activation over the North Pole. Here, we compute the total HCl concentration amount by using the natural abundance ratio of $H^{35}Cl$ and $H^{37}Cl$, i.e., $Cl^{35}/Cl^{37} = 0.7578/0.2422$.

Figure 6 depicts a comparison of observed TELIS spectra and modeled spectra corresponding to the first frequency segment. The relative residuals are within 4% at the lower tangent heights (19 and 22 km) with a maximum difference close to the center of the HCl line. The modeled spectra approximate the observed spectra better with increasing altitudes, albeit with larger discrepancies found in the line wings. By simulating the radiometric calibration process, the dip around the line center is also obtained in the modeled spectrum.

Figure 7 illustrates the individual estimates of smoothing, noise, and model parameters errors for the HCl retrieval. Between 22 and 32.5 km, the largest total error is about 0.3 ppbv. All independent errors steeply increase for altitudes below 20 km and from 30 km upwards. One explanation for larger errors around the lowest tangent height (16 km) could be that the nominal abundances (<1 ppbv) below 20 km are discovered and a reasonable retrieval below this altitude is rather difficult.

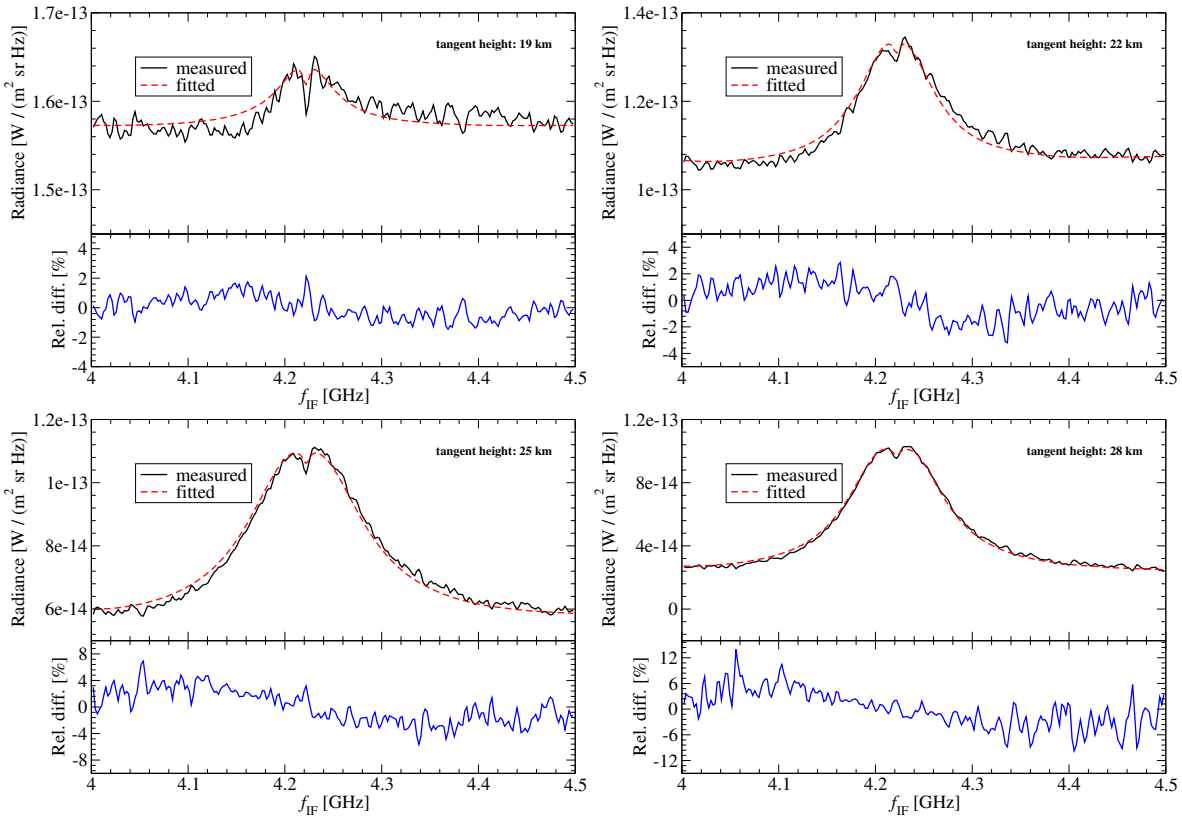

Figure 6. Comparison of the measured and modeled TELIS HCl spectra in segment 1. The dedicated measurement identifier is 20044 and the corresponding local oscillator frequency (f_{LO}) is 1877.6323 GHz. Four spectra are plotted for tangent heights at 19, 22, 25, and 28 km, respectively. For each tangent height, the relative differences with respect to the measured spectrum are shown in the bottom panel.

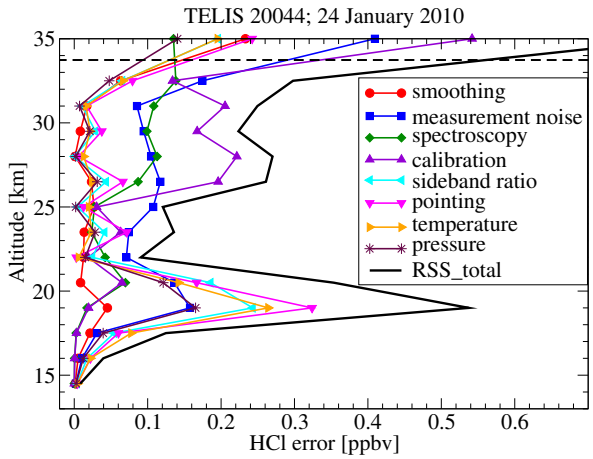

Figure 7. Individual estimates of smoothing, noise, and model parameters errors for HCl retrieval. The estimated errors correspond to TELIS FIR measurement 20044 during the 2010 flight.

Figure 8 depicts a retrieval comparison when both channels observed HCl simultaneously during the 2010 flight. The GHz-channel retrieval used both $H^{37}Cl$ and $H^{35}Cl$ transitions and was done by de Lange et al. [39]. Discrepancies resulting from a priori effects occurred between 16 and 21 km, whereas the good agreement above 23 km indicates the consistency of both channels.

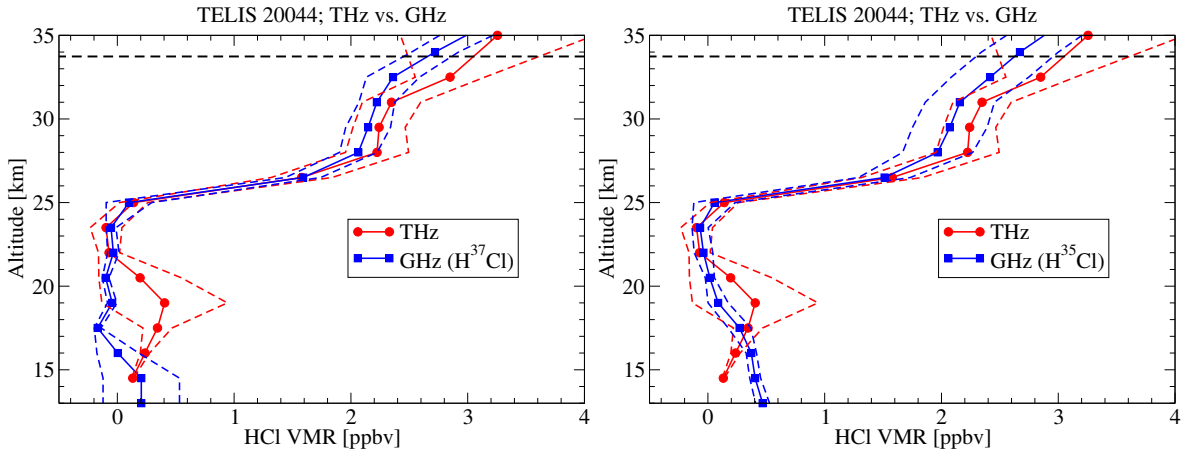

Figure 8. Comparison of HCl retrievals in the two channels of TELIS. The measurements have the same identifier (20044) and the two submillimeter profiles are derived from two different isotopes, i.e., $H^{37}Cl$ and $H^{35}Cl$, respectively.

This case also provides a chance to retrieve the molecule by joint processing of two spectral windows, such as the direct additive synergy [101]. Combined observations of the same variable lead to a better estimation, even though the measurement noise, the vertical resolution, and the altitude sensitivity can be different. The additive synergy needs to take into account the instrument noise level and spectral response function in each channel. Similar studies can be found in [102–104]. An experimental HCl retrieval in [60] indicated an improved retrieval accuracy and vertical sensitivity by the synergistic use of FIR and submillimeter synthetic spectra.

Figure 9 shows the HCl profile from multi-channel data using the additive synergy. It should be noted that the retrievals using the THz-channel data and the multi-channel data were performed by PILS, using the two $H^{37}Cl$ transitions located in the FIR and submillimeter microwindows, respectively. For reference, the profile retrieved from the GHz-channel data by de Lange et al. [39] is also included, with a DOFS of $\sim$7.3. The retrieval corresponding to a combination of the FIR and submillimeter microwindows agrees well with the GHz-channel profile at lower altitudes, whereas it tends towards to the THz-channel profile above 30 km. The averaging kernels broaden out at lower altitudes and above the balloon height due to the saturated spectra and few discernible HCl features. The kernels for the multi-channel fitting (Figure 9, bottom right) reveal a better vertical resolution than those for the THz-channel retrieval (Figure 9, bottom left) in the lower stratosphere, i.e., between 16 and 19 km. Presumably, in this altitude range, the information from the submillimeter signal can be complementary to the HCl retrieval. Furthermore, a gain in the DOFS is attained by the multi-channel fitting, showing that the retrieval sensitivity of HCl at lower altitudes in the submillimeter microwindow is superior to that in the FIR microwindow. Exploiting the complementary information provided by both channels can improve the HCl retrieval.

The full depletion of HCl in the lower stratosphere due to a strong chlorine activation inside the Northern Hemisphere polar vortex was seen by both instruments (see Figure 10). The HCl profiles from TELIS and MLS agree over most of the altitude range below 35 km. All possible error sources in the TELIS retrieval are taken into account, which can adequately explain why the MLS profile lies mostly within the accuracy bounds.

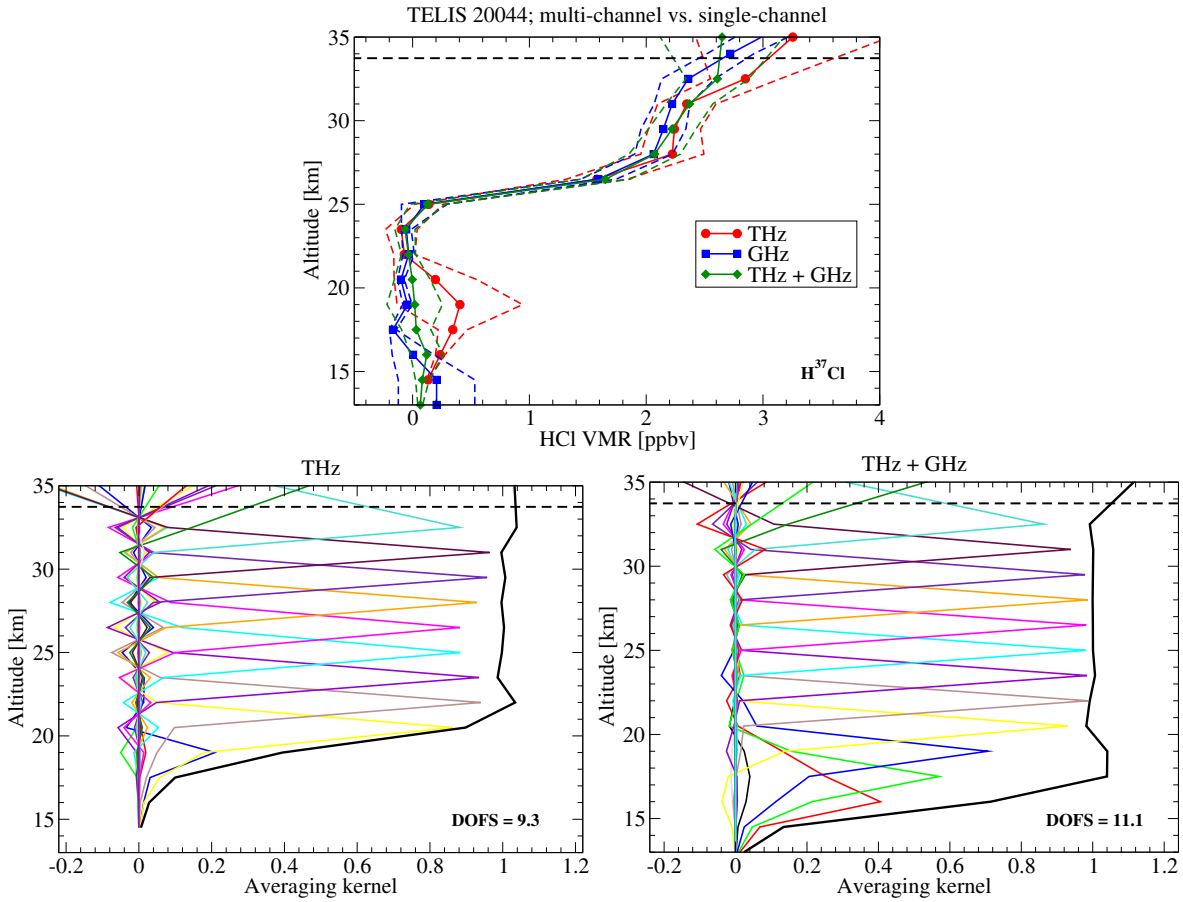

Figure 9. Retrieval result of HCl by using single- and multi-channel data of TELIS. Top panel: intercomparison of the retrieved HCl profile by using single- and multi-channel data. The HCl profile derived from the GHz-channel data is included for reference. Bottom panel: the corresponding averaging kernels and degree of freedom for the signal (DOFS) for the retrievals using single-channel (THz) data and for multi-channel data, respectively.

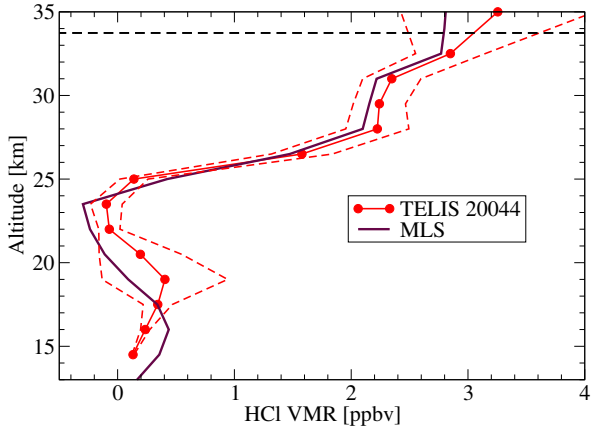

Figure 10. Comparison of HCl retrievals between TELIS and MLS on 24 January 2010. The lowest tangent height of TELIS is 16 km and the retrieval results below this altitude have little physical meaning. The solar zenith angle of the MLS measurement was 84.0°. The time difference between the TELIS and MLS measurements was about 0.1 h.

4.3. CO Retrieval

A limited number of CO limb scans were performed during these three flights. The retrievals for the 2010 flight are displayed in Figure 11. The balloon flight for these three measurements (from local morning to local noon) did not vary significantly (∼33–34 km) and the retrieved profiles resemble almost the same pattern. All retrieved CO profiles have a VMR of less than 0.1 ppmv in the stratosphere below 30 km and capture the peak at 32.5 km.

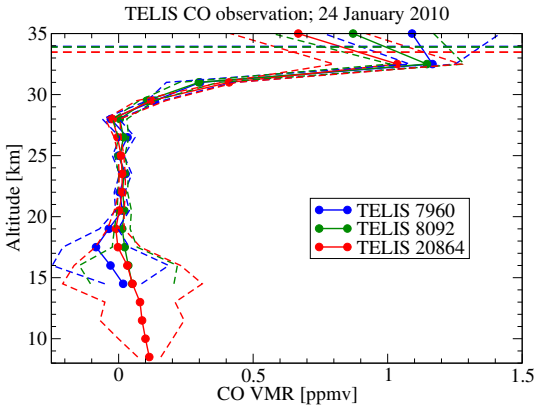

Figure 11. CO VMR profiles estimated from TELIS measurements on 24 January 2010.

A comparison of observed TELIS spectra and modeled spectra is shown in Figure 12. At the lower tangent height (17.5 km), the largest difference (5%) occurs around the line center. The largest differences for the other three tangent heights all occur around the intermediate frequency of 4.7 GHz.

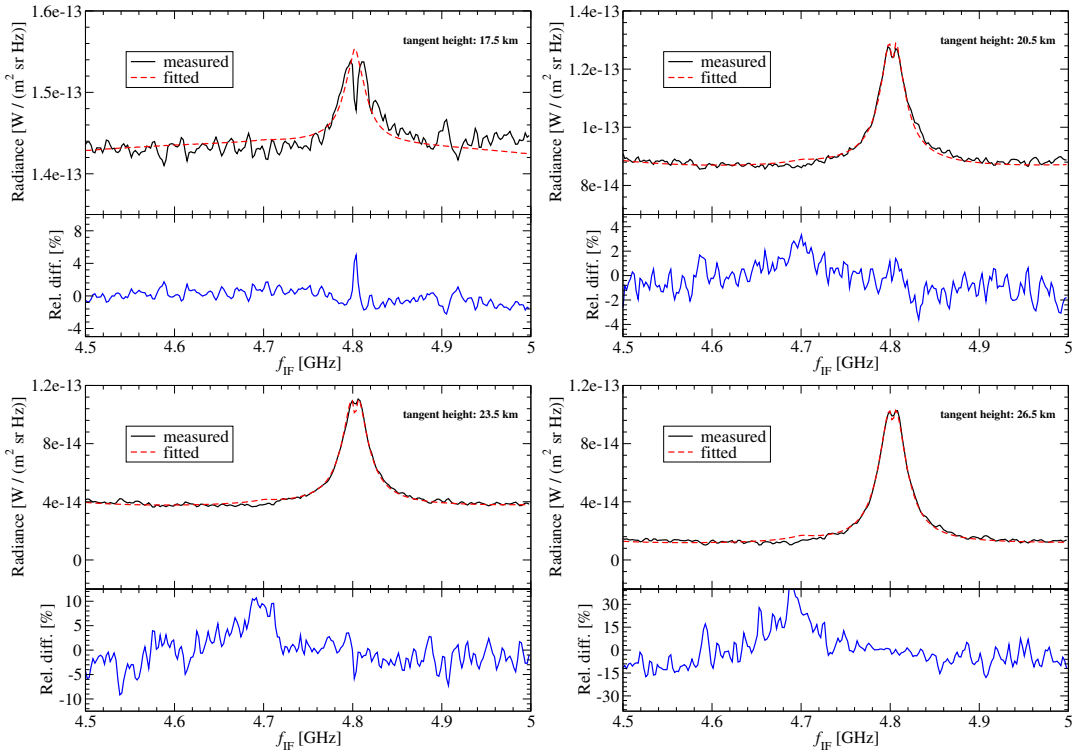

Figure 12. Comparison of measured and modeled TELIS CO spectra in segment 2. The dedicated measurement identifier is 20864 and the corresponding f_{LO} is 1836.5428 GHz. Four spectra are plotted for tangent heights at 17.5 km, 20.5 km, 22.5 km, and 26.5 km, respectively.

The averaging kernels and the values of DOFS for two CO retrievals from 2010 and 2011 TELIS data are shown in Figure 13. The vertical resolution is estimated to be about 1.8–3.5 km over the altitude range of 16–32.5 km, where the associated measurement response is greater than 0.8. The DOFS in both retrievals is greater than 10, suggesting the information in the stratosphere is mainly deduced from the measurement.

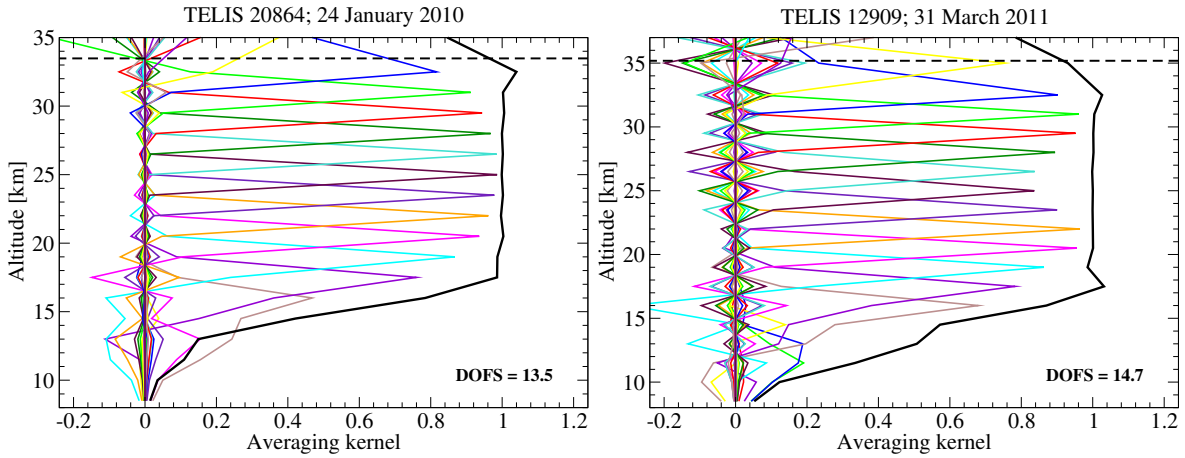

Figure 13. Averaging kernels and DOFS for the CO retrievals from TELIS FIR measurements 20864 (24 January 2010) and 12909 (31 March 2011), respectively.

The corresponding error propagation is displayed in Figure 14. At lower altitudes, the uncertainties in the temperature and pointing information turn out to be the two major error sources, with the peak appearing near 15 km. The measurement noise dominates the total error between 17.5 and 26.5 km, although the propagated noise error is only a bit larger than others. At higher altitudes, the spectroscopic parameters appear to be the most important error source. The total error is of about 0.01–0.25 ppmv.

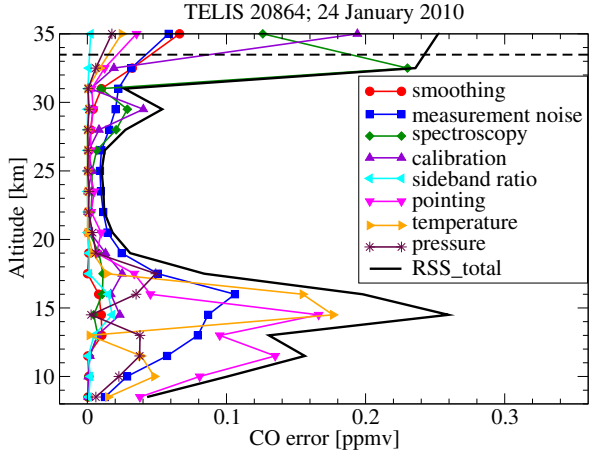

Figure 14. Individual estimates of smoothing, noise, and model parameters errors for the CO retrieval. The estimated errors correspond to TELIS FIR measurement 20864 during the 2010 flight.

One TELIS CO measurement was taken at local noon of 24 January 2010 and could be used to validate satellite measurements performed during a collocated overpass by the MLS instrument. In Figure 15, the CO profile retrieved from TELIS measurement 20864 is compared against the MLS profile. The two profiles were obtained within a small time interval (approximately 0.5 h) and a close geolocation. The difference in the solar zenith angle within 2° ensures that both sensors observed the same air mass around local noon on 24 January 2010. An excellent agreement can be seen in

both profiles and the peak at 32.5 km monitored by TELIS was also successfully captured by the MLS instrument. The MLS profile overall falls within the accuracy domain of the TELIS profile and both profiles show virtually identical shape.

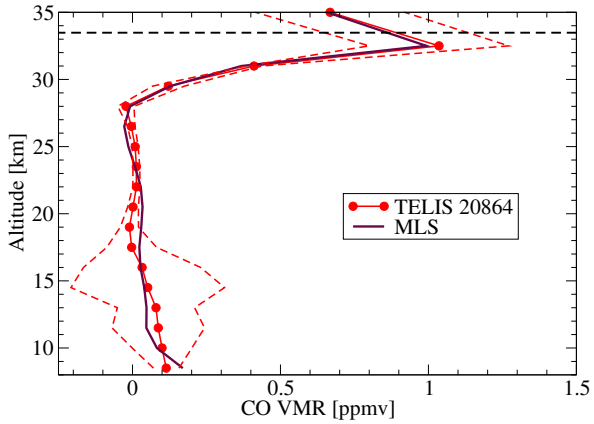

Figure 15. Comparison of CO retrievals from TELIS and MLS on 24 January 2010. The lowest tangent height of TELIS is 10 km and the retrieval results below this altitude have little physical meaning. The solar zenith angles of the MLS and TELIS data are 84.0° and 85.8°, respectively. The time difference of the TELIS and MLS measurements was less than 0.5 h.

4.4. OH Retrieval

In 2009, the TELIS instrument performed the regional measurements of OH during the time from local night to local morning, providing a chance to inquire into its diurnal variability.

The observed temporal evolution of OH concentration during the 2009 flight is displayed in Figure 16. On that day, the sunrise occurred around 06:00 h (UTC + 02:00). In total, 10 limb sequences (measured over five hours) with the observer altitude being above 20 km were analyzed. The time interval between adjacent TELIS measurements was not constant, producing a jump (discontinuous behavior) in the concentration level around 04:00 h UTC. At about 25 km, an increase can be noticed after sunrise. For most OH profiles shown in Figure 16, the abundances increase exponentially with altitude. The retrieved OH occasionally possesses oscillations in the stratosphere that are likely due to a very low contribution of OH at these altitudes to the recorded OH signal.

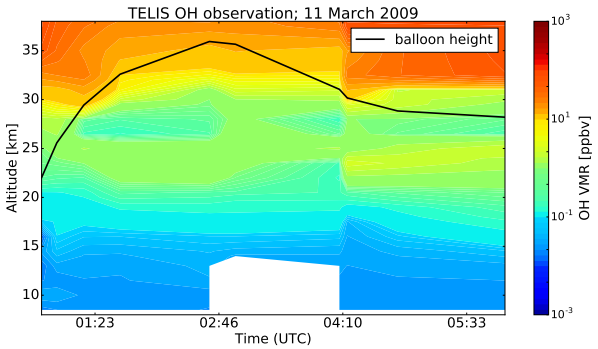

Figure 16. OH VMR profiles estimated from TELIS measurements on 11 March 2009. Here, the balloon height is indicated by a solid black line.

The comparison of measured and modeled spectra in segment 3 of the OH microwindow is shown in Figure 17. The relative differences between both spectra do not change dramatically (±1%) for the lower tangent heights of 13 and 17.5 km, and are of about ±2% for the tangent height at 22 km. At the higher tangent height of 26.5 km, the modeled spectrum is roughly ±8% off the measured spectrum

and the largest difference occurs near the intermediate frequency of about 5.5 GHz. The OH feature around the intermediate frequency of approximately 5.1 GHz is not very noticeable at lower tangent heights, but turns out to be stronger with the increasing tangent height.

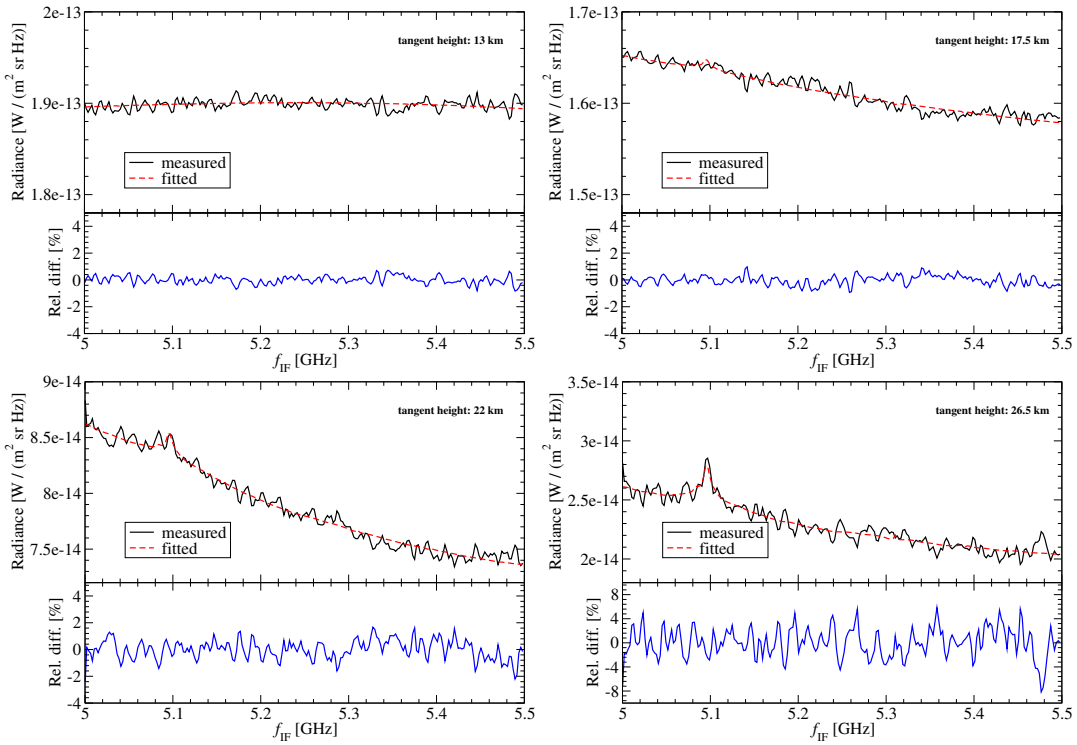

Figure 17. Comparison of measured and modeled TELIS OH spectra in segment 3. The dedicated measurement identifier is 10890 during the 2009 flight and the corresponding f_{LO} is 1829.6524 GHz. The spectra are plotted for tangent heights of 13 km, 17.5 km, 22 km, and 26.5 km.

The associated averaging kernels in Figure 18 indicate an enhanced retrieval sensitivity with increasing altitude. An increased measurement response is captured above 25 km where the OH abundances are larger by orders of magnitude. As can be seen from Figures 1 and 17, the OH feature below 20 km is contaminated by strong H_2O contributions, and therefore, its retrieval sensitivity becomes rather low in these regions.

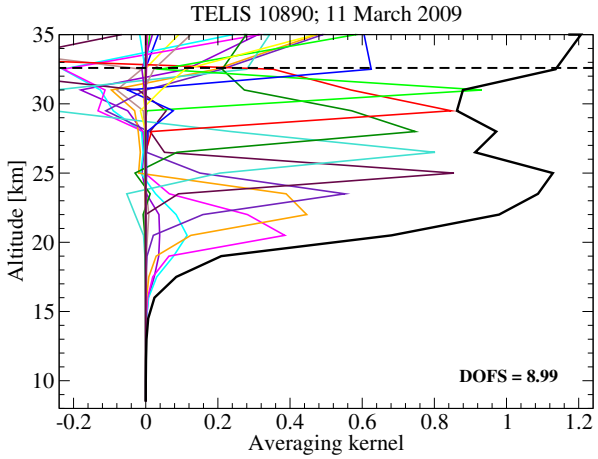

Figure 18. Averaging kernels and DOFS for the OH retrieval from TELIS FIR measurement 10890 (11 March 2009).

According to Figure 19, the retrieval error is less than 3 ppbv below 30 km and steadily increases at higher altitudes. Among the instrument parameters, the pointing accuracy appears to be crucial below 25 km. Only a limited number of available MIPAS-B temperature profiles were available in the 2009 flight, which can be problematic for TELIS retrieval. Despite that, the accuracy of temperature information turns out to be less important than other parameters. Spectroscopic parameters do not cause an obvious effect on the OH retrieval below the observer altitude. These findings are consistent with the sensitivity analysis in [60].

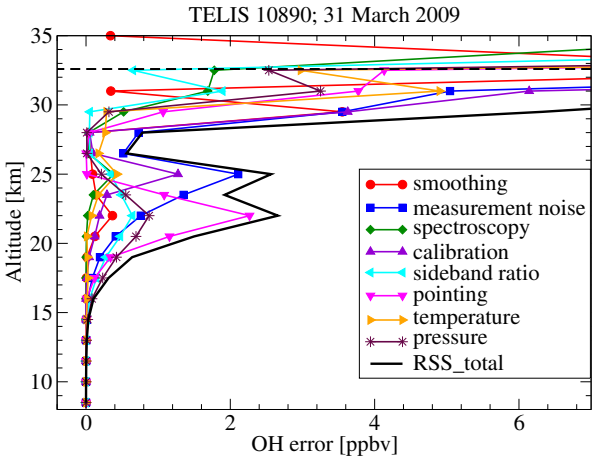

Figure 19. Individual estimates of smoothing, noise, and model parameters errors for the OH retrieval. The estimated errors correspond to TELIS FIR measurement 10890 during the 2009 flight.

In 2009, the THz module of MLS was placed in standby mode and has not been measuring OH regularly. In this study, there were no appropriate observations by other sensors used for the OH comparison.

5. Conclusions

The objective of this study was to analyze FIR limb spectra recorded by the balloon-borne spectrometer TELIS. Retrievals of stratospheric chemical species (O_3, HCl, CO, and OH) from TELIS spectra were presented, and their quality was analyzed in a quantitative manner. The following physical and diagnostic quantities were included for each molecule:

- concentration as a function of altitude;
- residual after convergence;
- retrieval diagnostics including an analysis of all considered error components and an averaging kernel matrix with DOFS.

O_3 profiles were retrieved by looking into different microwindows containing various ozone signatures. The retrieval sensitivity decreased when the altitude was higher than the balloon float altitude, indicating little information above the balloon. Strong H_2O contamination and low O_3 abundance led to a lower retrieval sensitivity in the upper troposphere. An intercomparison of VMR profiles between TELIS and MIPAS-B during the 2010 and 2011 flights proved the internal consistency of the two instruments on the same platform. Moreover, two TELIS profiles from the 2010 flight were compared against three spaceborne observations, showing a remarkable overall agreement.

HCl retrievals were performed from the TELIS data during the 2010 flight which took place inside the activated Arctic vortex. A comparison between the THz and GHz channels confirmed the internal consistency of TELIS, whereas comparisons with the coincident SMILES and MLS profiles agreed well within the accuracy domain of the TELIS profile. Further, a retrieval by the synergistic use of FIR and submillimeter measurements demonstrated a promising attempt to exploit more useful information

from extended spectral ranges. The inversion diagnostic quantifiers indicate that the retrieval quality and sensitivity can be enhanced.

CO retrievals at lower altitudes can be affected by the uncertainties in the temperature and pointing information. A TELIS profile retrieved from the 2010 flight was compared against the MLS data and an excellent agreement was found over the altitude range of interest for TELIS. The vertical resolution of the TELIS retrieval was 2–3.5 km between 16 and 32.5 km, where the corresponding measurement response was greater than 0.8.

First, OH retrievals from TELIS measurements with a vertical resolution of about 4–5 km were conducted for the 2009 flight. The retrieval sensitivity appeared to be very low below 20 km, where the OH signal was contaminated by water continua. The dominant error sources below the observer altitude are the pointing uncertainty and the measurement noise. Consequently, the retrieval performance of OH can be improved by a better characterization of the instrument.

According to the error analysis, the measurement noise turned out to be a severe error source in the 1.8-THz channel, which was not unexpected. The errors due to the uncertainties in the instrument knowledge and pressure profile were dominant in the upper troposphere and lower stratosphere, whereas the retrieval errors at higher altitudes were mostly due to the uncertainties in the spectroscopy and the calibration. In conjunction with the internal and external comparisons, the error analysis serves to improve our understanding of the TELIS measurement characteristics.

The TELIS balloon-borne measurements provide snapshot type profile products of satisfactory vertical resolution and encouraging retrieval accuracy. An important lesson learned from this analysis of the TELIS data with regard to future projects/missions is the importance and necessity of a thorough pre-launch/laboratory characterization of the instrument. The measurement noise was very low in the 480–650 GHz channel and did not greatly affect the retrieval precision [39], but it turned out to be a discernible error source in the 1.8-THz channel. Among considered instrument parameters, the pointing accuracy appears to be critical at lower altitudes, whereas the accuracies of the other parameters (calibration, spectral noise) that are not severe at lower altitudes become dominant at higher altitudes.

The quality of the TELIS retrievals is in line with pre-launch expectations of the instrument performance and manifests its capability for observing atmospheric minor constituents in the upper troposphere and stratosphere. The retrieved TELIS profiles are consistent with the ones obtained by other limb-sounding sensors.

Retrieval of OH could be a challenging scientific problem on its own, and other instruments measuring it reliably might be difficult to find. Further investigations into an optimal retrieval strategy and the validation of TELIS OH profiles are required.

Future projects include the ALTIUS (Belgian) mission covering the UV, visible, and near infrared spectral regions, which can measure ozone profiles, but not the wealth of species that can be obtained from the FIR/TIR or microwave spectral regions. Unfortunately, no European spaceborne limb emission sounder (like MLS, SMILES) is scheduled for launch in the near future. Hence, balloon and airborne sensors can be used as economical alternatives focusing on the vertical structure of stratospheric compositions.

Acknowledgments: The work of J. Xu was partly funded by the German Academic Exchange Service (DAAD). The authors appreciate the three anonymous reviewers for providing numerous valuable suggestions that led to a better-organized manuscript. The authors would like to thank P. Vogt and O. Kiselev for their work on processing the TELIS calibrated radiance spectra during their time at the DLR. The authors would also thank the L2 data processing teams from KIT, NICT, and JPL for providing the retrieved atmospheric profiles measured by MIPAS-B, SMILES, and MLS. The authors are grateful to J. Landgraf (SRON) and H. Oelhaf (KIT) for many fruitful discussions and suggestions on the retrieval concept during prior TELIS/MIPAS-B science meetings. Thanks are given to J.L. Grenfell for proofreading the manuscript.

Author Contributions: J. Xu and F. Schreier developed the software for TELIS L2 processing, and conceived and designed the retrieval framework; J. Xu performed the retrievals, analyzed the data, and prepared the manuscript; G. Wetzel and A. de Lange contributed to the evaluation and intercomparison of the TELIS L2 results; M. Birk and G. Wagner contributed to the TELIS instrument development and provided L1 data; F. Schreier, T. Trautmann,

and A. Doicu contributed in many scientific discussions on the overall development of the TELIS L2 project. All co-authors read the manuscript and provided comments.

Conflicts of Interest: The authors declare no conflict of interest.

References

1. Harries, J.; Carli, B.; Rizzi, R.; Serio, C.; Mlynczak, M.; Palchetti, L.; Maestri, T.; Brindley, H.; Masiello, G. The Far-infrared Earth. *Rev. Geophys.* **2008**, *46*, doi:10.1029/2007RG000233.
2. Carli, B.; Mencaraglia, F.; Bonetti, A. Submillimeter high-resolution FT spectrometer for atmospheric studies. *Appl. Opt.* **1984**, *23*, 2594–2603.
3. Carli, B.; Park, J.H. Simultaneous measurement of minor stratospheric constituents with emission far-infrared spectroscopy. *J. Geophys. Res. Atmos.* **1988**, *93*, 3851–3865.
4. Carli, B.; Mencaraglia, F.; Carlotti, M.; Dinelli, B.M.; Nolt, I. Submillimeter measurements of stratospheric chlorine monoxide. *J. Geophys. Res. Atmos.* **1988**, *93*, 7063–7068.
5. Carli, B.; Carlotti, M.; Dinelli, B.; Mencaraglia, F.; Park, J. The mixing ratio of stratospheric hydroxyl radical from far infrared emission measurements. *J. Geophys. Res.* **1989**, *94*, 11049–11058.
6. Carlotti, M.; Barbis, A.; Carli, B. Stratospheric ozone vertical distribution from far-infrared balloon spectra and statistical analysis of the errors. *J. Geophys. Res. Atmos.* **1989**, *94*, 16365–16372.
7. Barath, F.T.; Chavez, M.C.; Cofield, R.E.; Flower, D.A.; Frerking, M.A.; Gram, M.B.; Harris, W.M.; Holden, J.R.; Jarnot, R.F.; Kloezeman, W.G.; et al. The Upper Atmosphere Research Satellite microwave limb sounder instrument. *J. Geophys. Res.* **1993**, *98*, 10751–10762.
8. Murtagh, D.; Frisk, U.; Merino, F.; Ridal, M.; Jonsson, A.; Stegman, J.; Witt, G.; Eriksson, P.; Jiménez, C.; Megie, G.; et al. An overview of the Odin atmospheric mission. *Can. J. Phys.* **2002**, *80*, 309–319.
9. Waters, J.; Froidevaux, L.; Harwood, R.; Jarnot, R.; Pickett, H.; Read, W.; Siegel, P.; Cofield, R.; Filipiak, M.; Flower, D.; et al. The Earth Observing System Microwave Limb Sounder (EOS MLS) on the Aura satellite. *IEEE Trans. Geosci. Remote Sens.* **2006**, *44*, 1075–1092.
10. Kikuchi, K.; Nishibori, T.; Ochiai, S.; Ozeki, H.; Irimajiri, Y.; Kasai, Y.; Koike, M.; Manabe, T.; Mizukoshi, K.; Murayama, Y.; et al. Overview and early results of the Superconducting Submillimeter-Wave Limb-Emission Sounder (SMILES). *J. Geophys. Res. Atmos.* **2010**, *115*, doi:10.1029/2010JD014379.
11. Johnson, D.G.; Jucks, K.W.; Traub, W.A.; Chance, K.V. Smithsonian stratospheric far-infrared spectrometer and data reduction system. *J. Geophys. Res. Atmos.* **1995**, *100*, 3091–3106.
12. Chance, K.; Johnson, D.; Traub, W. Measurement of stratospheric HOCl: Concentration profiles, including diurnal variation. *J. Geophys. Res. Atmos.* **1989**, *94*, 11059–11069.
13. Traub, W.A.; Johnson, D.G.; Chance, K.V. Stratospheric Hydroperoxyl Measurements. *Science* **1990**, *247*, 446–449.
14. Chance, K.V.; Johnson, D.G.; Traub, W.A.; Jucks, K.W. Measurement of the stratospheric hydrogen peroxide concentration profile using far infrared thermal emission spectroscopy. *Geophys. Res. Lett.* **1991**, *18*, 1003–1006.
15. Jucks, K.; Johnson, D.; Chance, K.; Traub, W.; Margitan, J.; Osterman, G.; Salawitch, R.; Sasano, Y. Observations of OH, HO_2, H_2O, and O_3 in the upper stratosphere: Implications for HO_x photochemistry. *Geophys. Res. Lett.* **1998**, *25*, 3935–3938.
16. Friedl-Vallon, F.; Maucher, G.; Seefeldner, M.; Trieschmann, O.; Kleinert, A.; Lengel, A.; Keim, C.; Oelhaf, H.; Fischer, H. Design and characterization of the balloon-borne Michelson Interferometer for Passive Atmospheric Sounding (MIPAS-B2). *Appl. Opt.* **2004**, *43*, 3335–3355.
17. Fischer, H.; Birk, M.; Blom, C.; Carli, B.; Carlotti, M.; von Clarmann, T.; Delbouille, L.; Dudhia, A.; Ehhalt, D.; Endemann, M.; et al. MIPAS: An instrument for atmospheric and climate research. *Atmos. Chem. Phys.* **2008**, *8*, 2151–2188.
18. Höpfner, M.; von Clarmann, T.; Fischer, H.; Funke, B.; Glatthor, N.; Grabowski, U.; Kellmann, S.; Kiefer, M.; Linden, A.; Milz, M.; et al. Validation of MIPAS $ClONO_2$ measurements. *Atmos. Chem. Phys.* **2007**, *7*, 257–281.
19. Wang, D.Y.; Höpfner, M.; Blom, C.E.; Ward, W.E.; Fischer, H.; Blumenstock, T.; Hase, F.; Keim, C.; Liu, G.Y.; Mikuteit, S.; et al. Validation of MIPAS HNO_3 operational data. *Atmos. Chem. Phys.* **2007**, *7*, 4905–4934.
20. Wetzel, G.; Bracher, A.; Funke, B.; Goutail, F.; Hendrick, F.; Lambert, J.C.; Mikuteit, S.; Piccolo, C.; Pirre, M.; Bazureau, A.; et al. Validation of MIPAS-ENVISAT NO_2 operational data. *Atmos. Chem. Phys.* **2007**, *7*, 3261–3284.

21. Zhang, G.; Wetzel, G.; Oelhaf, H.; Friedl-Vallon, F.; Kleinert, A.; Lengel, A.; Maucher, G.; Nordmeyer, H.; Grunow, K.; Fischer, H. Validation of temperature measurements from MIPAS-ENVISAT with balloon observations obtained by MIPAS-B. *J. Atmos. Sol.-Terr. Phys.* **2010**, *72*, 837–847.
22. Zhang, G.; Wetzel, G.; Oelhaf, H.; Friedl-Vallon, F.; Kleinert, A.; Lengel, A.; Maucher, G.; Nordmeyer, H.; Grunow, K.; Fischer, H. Validation of atmospheric chemistry measurements from MIPAS, SCIAMACHY, GOMOS onboard ENVISAT by observations of balloon-borne MIPAS-B. *Sci. China Earth Sci.* **2010**, *53*, 1533–1541.
23. Wetzel, G.; Oelhaf, H.; Berthet, G.; Bracher, A.; Cornacchia, C.; Feist, D.G.; Fischer, H.; Fix, A.; Iarlori, M.; Kleinert, A.; et al. Validation of MIPAS-ENVISAT H_2O operational data collected between July 2002 and March 2004. *Atmos. Chem. Phys.* **2013**, *13*, 5791–5811.
24. Wetzel, G.; Oelhaf, H.; Friedl-Vallon, F.; Kleinert, A.; Lengel, A.; Maucher, G.; Nordmeyer, H.; Ruhnke, R.; Nakajima, H.; Sasano, Y.; et al. Intercomparison and validation of ILAS-II version 1.4 target parameters with MIPAS-B measurements. *J. Geophys. Res. Atmos.* **2006**, *111*, doi:10.1029/2005JD006287.
25. Sagawa, H.; Sato, T.O.; Baron, P.; Dupuy, E.; Livesey, N.; Urban, J.; von Clarmann, T.; de Lange, A.; Wetzel, G.; Connor, B.J.; et al. Comparison of SMILES ClO profiles with satellite, balloon-borne and ground-based measurements. *Atmos. Meas. Tech.* **2013**, *6*, 3325–3347.
26. Camy-Peyret, C.; Jeseck, P.; Hawat, T.; Durry, G.; Payan, S.; Berubé, G.; Rochette, L.; Huguenin, D. The LPMA balloon-borne FTIR spectrometer for remote sensing of atmospheric constituents. In Proceedings of the 12th ESA Symposium on European Rocket and Balloon Programmes and Related Research, Lillehammer, Norway, 29 May–1 June 1995; Kaldeich-Schürmann, B., Ed.; ESA Special Publication: Paris, France, 1995; SP-370, pp. 323–328.
27. Irimajiri, Y.; Manabe, T.; Ochiai, S.; Masuko, H.; Yamagami, T.; Saito, Y.; Izutsu, N.; Kawasaki, T.; Namiki, M.; Murata, I. BSMILES—A balloon-borne superconducting submillimeter-wave limb-emission sounder for stratospheric measurements. *IEEE Geosci. Remote Sens. Lett.* **2006**, *3*, 88–92.
28. Waters, J.; Hardy, J.; Jarnot, R.; Pickett, H.; Zimmerman, P. A balloon-borne microwave limb sounder for stratospheric measurements. *J. Quant. Spectrosc. Radiat. Transf.* **1984**, *32*, 407–433.
29. Birk, M.; Wagner, G.; de Lange, G.; de Lange, A.; Ellison, B.N.; Harman, M.R.; Murk, A.; Oelhaf, H.; Maucher, G.; Sartorius, C. TELIS: TErahertz and subMMW LImb Sounder—Project Summary After First Sucessful Flight. In Proceedings of the 21st International Symposium on Space Terahertz Technology, Oxford and Didcot, UK, 23–25 March 2010; University of Oxford and STFC Rutherford Appleton Laboratory: Swindon, UK, 2010; pp. 195–200.
30. Suttiwong, N.; Birk, M.; Wagner, G.; Krocka, M.; Wittkamp, M.; Haschberger, P.; Vogt, P.; Geiger, F. Development and characterization of the balloon borne instrument TELIS (TEhertz and Submm LImb Sounder): 1.8 THz receiver. In Proceedings of the 19th ESA Symposium on European Rocket and Balloon Programmes and Related Research, Bad Reichenhall, Germany, 7–11 June 2009.
31. De Lange, G.; Birk, M.; Boersma, D.; Derckson, J.; Dmitriev, P.; Ermakov, A.; Filippenko, L.; Golstein, H.; Hoogeveen, R.; de Jong, L.; et al. Development and characterization of the superconducting integrated receiver channel of the TELIS atmospheric sounder. *Supercond. Sci. Technol.* **2010**, *23*, doi:10.1088/0953-2048/23/4/045016.
32. Kasai, Y.; Sagawa, H.; Kreyling, D.; Dupuy, E.; Baron, P.; Mendrok, J.; Suzuki, K.; Sato, T.O.; Nishibori, T.; Mizobuchi, S.; et al. Validation of stratospheric and mesospheric ozone observed by SMILES from International Space Station. *Atmos. Meas. Tech.* **2013**, *6*, 2311–2338.
33. Eckert, E.; Laeng, A.; Lossow, S.; Kellmann, S.; Stiller, G.; von Clarmann, T.; Glatthor, N.; Höpfner, M.; Kiefer, M.; Oelhaf, H.; et al. MIPAS IMK/IAA CFC-11 (CCl_3F) and CFC-12 (CCl_2F_2) measurements: Accuracy, precision and long-term stability. *Atmos. Meas. Tech.* **2016**, *9*, 3355–3389.
34. Koshelets, V.P.; Ermakov, A.B.; Filippenko, L.V.; Khudchenko, A.V.; Kiselev, O.S.; Sobolev, A.S.; Torgashin, M.Y.; Yagoubov, P.A.; Hoogeveen, R.W.M.; Wild, W. Superconducting Integrated Submillimeter Receiver for TELIS. *IEEE Trans. Appl. Supercond.* **2007**, *17*, 336–342.
35. Kiselev, O.; Birk, M.; Ermakov, A.; Filippenko, L.; Golstein, H.; Hoogeveen, R.; Kinev, N.; van Kuik, B.; de Lange, A.; de Lange, G.; et al. Balloon-borne superconducting integrated receiver for atmospheric research. *IEEE Trans. Appl. Supercond.* **2011**, *21*, 612–615.

36. Koshelets, V.P.; Dmitriev, P.N.; Faley, M.I.; Filippenko, L.V.; Kalashnikov, K.V.; Kinev, N.V.; Kiselev, O.S.; Artanov, A.A.; Rudakov, K.I.; de Lange, A.; et al. Superconducting Integrated Terahertz Spectrometers. *IEEE Trans. Terahertz Sci. Technol.* **2015**, *5*, 687–694.
37. Kiselev, O.S.; Ermakov, A.B.; Koshelets, V.P.; Filippenko, L.V. Application of superconducting integrated receiver in the TELIS instrument for the spectroscopic study of atmosphere. *J. Commun. Technol. Electron.* **2016**, *61*, 1314–1319.
38. De Lange, A.; Landgraf, J.; Hoogeveen, R. Stratospheric isotopic water profiles from a single submillimeter limb scan by TELIS. *Atmos. Meas. Tech.* **2009**, *2*, 423–435.
39. De Lange, A.; Birk, M.; de Lange, G.; Friedl-Vallon, F.; Kiselev, O.; Koshelets, V.; Maucher, G.; Oelhaf, H.; Selig, A.; Vogt, P.; et al. HCl and ClO in activated Arctic air; first retrieved vertical profiles from TELIS submillimetre limb spectra. *Atmos. Meas. Tech.* **2012**, *5*, 487–500.
40. Pickett, H. Microwave Limb Sounder THz module on Aura. *IEEE Trans. Geosci. Remote Sens.* **2006**, *44*, 1122–1130.
41. Englert, C.; Schimpf, B.; Birk, M.; Schreier, F.; Krocka, M.; Nitsche, R.; Titz, R.; Summers, M. The 2.5 THz heterodyne spectrometer THOMAS: Measurement of OH in the middle atmosphere and comparison with photochemical model results. *J. Geophys. Res. Atmos.* **2000**, *105*, 22211–22223.
42. Carlotti, M.; Ade, P.; Carli, B.; Chipperfield, M.; Hamilton, P.; Mencaraglia, F.; Nolt, I.; Ridolfi, M. Diurnal variability and night detection of stratospheric hydroxyl radical from far infrared emission measurements. *J. Atmos. Sol.-Terr. Phys.* **2001**, *63*, 1509–1518.
43. Pickett, H.M.; Peterson, D.B. Stratospheric OH measurements with a far-infrared limb observing spectrometer. *J. Geophys. Res. Atmos.* **1993**, *98*, 20507–20515.
44. Von Hobe, M.; Bekki, S.; Borrmann, S.; Cairo, F.; D'Amato, F.; Di Donfrancesco, G.; Dörnbrack, A.; Ebersoldt, A.; Ebert, M.; Emde, C.; et al. Reconciliation of essential process parameters for an enhanced predictability of Arctic stratospheric ozone loss and its climate interactions (RECONCILE): Activities and results. *Atmos. Chem. Phys.* **2013**, *13*, 9233–9268.
45. Zhang, J.; Tian, W.; Chipperfield, M.P.; Xie, F.; Huang, J. Persistent shift of the Arctic polar vortex towards the Eurasian continent in recent decades. *Nat. Clim. Chang.* **2016**, *6*, 1094–1099.
46. Arnone, E.; Castelli, E.; Papandrea, E.; Carlotti, M.; Dinelli, B.M. Extreme ozone depletion in the 2010–2011 Arctic winter stratosphere as observed by MIPAS/ENVISAT using a 2-D tomographic approach. *Atmos. Chem. Phys.* **2012**, *12*, 9149–9165.
47. Sagi, K.; Murtagh, D.; Urban, J.; Sagawa, H.; Kasai, Y. The use of SMILES data to study ozone loss in the Arctic winter 2009/2010 and comparison with Odin/SMR data using assimilation techniques. *Atmos. Chem. Phys.* **2014**, *14*, 12855–12869.
48. Woiwode, W.; Oelhaf, H.; Gulde, T.; Piesch, C.; Maucher, G.; Ebersoldt, A.; Keim, C.; Höpfner, M.; Khaykin, S.; Ravegnani, F.; et al. MIPAS-STR measurements in the Arctic UTLS in winter/spring 2010: Instrument characterization, retrieval and validation. *Atmos. Meas. Tech.* **2012**, *5*, 1205–1228.
49. Castelli, E.; Dinelli, B.M.; Del Bianco, S.; Gerber, D.; Moyna, B.P.; Siddans, R.; Kerridge, B.J.; Cortesi, U. Measurement of the Arctic UTLS composition in presence of clouds using millimetre-wave heterodyne spectroscopy. *Atmos. Meas. Tech.* **2013**, *6*, 2683–2701.
50. Jacobson, M.Z. *Air Pollution and Global Warming: History, Science, and Solutions*, 2nd ed.; Cambridge University Press: New York, NY, USA, 2012.
51. Wetzel, G.; Oelhaf, H.; Kirner, O.; Friedl-Vallon, F.; Ruhnke, R.; Ebersoldt, A.; Kleinert, A.; Maucher, G.; Nordmeyer, H.; Orphal, J. Diurnal variations of reactive chlorine and nitrogen oxides observed by MIPAS-B inside the January 2010 Arctic vortex. *Atmos. Chem. Phys.* **2012**, *12*, 6581–6592.
52. Wetzel, G.; Oelhaf, H.; Birk, M.; de Lange, A.; Engel, A.; Friedl-Vallon, F.; Kirner, O.; Kleinert, A.; Maucher, G.; Nordmeyer, H.; et al. Partitioning and budget of inorganic and organic chlorine species observed by MIPAS-B and TELIS in the Arctic in March 2011. *Atmos. Chem. Phys.* **2015**, *15*, 8065–8076.
53. Allen, D.R.; Stanford, J.L.; López-Valverde, M.A.; Nakamura, N.; Lary, D.J.; Douglass, A.R.; Cerniglia, M.C.; Remedios, J.J.; Taylor, F.W. Observations of middle atmosphere CO from the UARS ISAMS during the early northern winter 1991/92. *J. Atmos. Sci.* **1999**, *56*, 563–583.
54. Wehr, T.; Bühler, S.; von Engeln, A.; Künzi, K.; Langen, J. Retrieval of stratospheric temperatures from spaceborne microwave limb sounding measurement. *J. Geophys. Res. Atmos.* **1998**, *103*, 25997–26006.

55. Von Engeln, A.; Langen, J.; Wehr, T.; Bühler, S.; Künzi, K. Retrieval of upper stratospheric and mesospheric temperature profiles from Millimeter-Wave Atmospheric Sounder data. *J. Geophys. Res. Atmos.* **1998**, *103*, 31735–31748.
56. Carlotti, M.; Ridolfi, M. Derivation of temperature and pressure from submillimetric limb observations. *Appl. Opt.* **1999**, *38*, 2398–2409.
57. Verdes, C.; Bühler, S.; von Engeln, A.; Kuhn, T.; Künzi, K.; Eriksson, P.; Sinnhuber, B.M. Pointing and temperature retrieval from millimeter–submillimeter limb soundings. *J. Geophys. Res. Atmos.* **2002**, *107*, ACH 10-1–ACH 10-24.
58. Von Engeln, A.; Bühler, S. Temperature profile determination from microwave oxygen emissions in limb sounding geometry. *J. Geophys. Res. Atmos.* **2002**, *107*, ACL 12-1–ACL 12-15.
59. Suttiwong, N. Development and Characteristics of the Balloon Borne Instrument TELIS (TEhertz and Submillimeter LImb Sounder): 1.8 THz Receiver. PhD Thesis, University of Bremen, Bremen, Germany, 25 October 2010.
60. Xu, J.; Schreier, F.; Vogt, P.; Doicu, A.; Trautmann, T. A sensitivity study for far infrared balloon-borne limb emission sounding of stratospheric trace gases. *Geosci. Instrum. Methods Data Syst. Discuss.* **2013**, *3*, 251–303.
61. Xu, J. Inversion for Limb Infrared Atmospheric Sounding. PhD Thesis, Technische Universität München, Munich, Germany, 9 May 2015.
62. Schreier, F.; Gimeno García, S.; Hedelt, P.; Hess, M.; Mendrok, J.; Vasquez, M.; Xu, J. GARLIC—A general purpose atmospheric radiative transfer line-by-line infrared-microwave code: Implementation and evaluation. *J. Quant. Spectrosc. Radiat. Transf.* **2014**, *137*, 29–50.
63. Doicu, A.; Schreier, F.; Hilgers, S.; Hess, M. Multi-parameter regularization method for atmospheric remote sensing. *Comput. Phys. Commun.* **2005**, *165*, 1–9.
64. Dennis, J., Jr.; Schnabel, R.B. *Numerical Methods for Unconstrained Optimization and Nonlinear Equations*; SIAM: Philadelphia, PA, USA, 1996.
65. Griewank, A.; Walther, A. *Evaluating Derivatives: Principles and Techniques of Algorithmic Differentiation*, 2nd ed.; SIAM: Philadelphia, PA, USA, 2008.
66. Neidinger, R.D. Introduction to Automatic Differentiation and MATLAB Object-Oriented Programming. *SIAM Rev.* **2010**, *52*, 545–563.
67. Schreier, F.; Gimeno García, S.; Vasquez, M.; Xu, J. Algorithmic vs. finite difference Jacobians for infrared atmospheric radiative transfer. *J. Quant. Spectrosc. Radiat. Transf.* **2015**, *164*, 147–160.
68. Hascoët, L.; Pascual, V. The Tapenade Automatic Differentiation tool: Principles, Model, and Specification. *ACM Trans. Math. Softw.* **2013**, *39*, doi:10.1145/2450153.2450158.
69. Bakushinskii, A. The problem of the convergence of the iteratively regularized Gauss–Newton method. *Comput. Math. Math. Phys.* **1992**, *32*, 1353–1359.
70. Doicu, A.; Schreier, F.; Hess, M. Iteratively Regularized Gauss–Newton Method for Atmospheric Remote Sensing. *Comput. Phys. Commun.* **2002**, *148*, 214–226.
71. Morozov, V.A. On the solution of functional equations by the method of regularization. *Sov. Math. Dokl.* **1966**, *7*, 414–417.
72. Engl, H.W. Discrepancy principles for Tikhonov regularization of ill-posed problems leading to optimal convergence rates. *J. Optim. Theory Appl.* **1987**, *52*, 209–215.
73. Xu, J.; Schreier, F.; Doicu, A.; Trautmann, T. Assessment of Tikhonov-type regularization methods for solving atmospheric inverse problems. *J. Quant. Spectrosc. Radiat. Transf.* **2016**, *184*, 274–286.
74. Wetzel, G.; Oelhaf, H.; Ruhnke, R.; Friedl-Vallon, F.; Kleinert, A.; Kouker, W.; Maucher, G.; Reddmann, T.; Seefeldner, M.; Stowasser, M.; et al. NO_y partitioning and budget and its correlation with N_2O in the Arctic vortex and in summer midlatitudes in 1997. *J. Geophys. Res. Atmos.* **2002**, *107*, ACH 3-1–ACH 3-10.
75. Anderson, G.; Clough, S.; Kneizys, F.; Chetwynd, J.; Shettle, E. *AFGL Atmospheric Constituent Profiles (0–120 km)*; Technical Report TR-86-0110; AFGL: Palm Desert, CA, USA, 15 May 1986.
76. Clough, S.; Kneizys, F.; Davies, R. Line Shape and the Water Vapor Continuum. *Atmos. Res.* **1989**, *23*, 229–241.
77. Rothman, L.; Gordon, I.; Babikov, Y.; Barbe, A.; Benner, D.C.; Bernath, P.; Birk, M.; Bizzocchi, L.; Boudon, V.; Brown, L.; et al. The HITRAN2012 molecular spectroscopic database. *J. Quant. Spectrosc. Radiat. Transf.* **2013**, *130*, 4–50.
78. Rinsland, C.P.; Zander, R.; Namkung, J.S.; Farmer, C.B.; Norton, R.H. Stratospheric infrared continuum absorptions observed by the ATMOS experiment. *J. Geophys. Res. Atmos.* **1989**, *94*, 16303–16322.

79. Ridolfi, M.; Carli, B.; Carlotti, M.; Clarmann, T.V.; Dinelli, B.M.; Dudhia, A.; Flaud, J.M.; Höpfner, M.; Morris, P.E.; Raspollini, P.; et al. Optimized forward model and retrieval scheme for MIPAS near-real-time data processing. *Appl. Opt.* **2000**, *39*, 1323–1340.
80. Stiller, G.; von Clarmann, T.; Funke, B.; Glatthor, N.; Hase, F.; Höpfner, M.; Linden, A. Sensitivity of trace gas abundances retrievals from infrared limb emission spectra to simplifying approximations in radiative transfer modelling. *J. Quant. Spectrosc. Radiat. Transf.* **2002**, *72*, 249–280.
81. Boone, C.D.; Nassar, R.; Walker, K.A.; Rochon, Y.; McLeod, S.D.; Rinsland, C.P.; Bernath, P.F. Retrievals for the atmospheric chemistry experiment Fourier-transform spectrometer. *Appl. Opt.* **2005**, *44*, 7218–7231.
82. Baron, P.; Urban, J.; Sagawa, H.; Möller, J.; Murtagh, D.P.; Mendrok, J.; Dupuy, E.; Sato, T.O.; Ochiai, S.; Suzuki, K.; et al. The Level 2 research product algorithms for the Superconducting Submillimeter-Wave Limb-Emission Sounder (SMILES). *Atmos. Meas. Tech.* **2011**, *4*, 2105–2124.
83. Urban, J.; Lautié, N.; Flochmoën, E.L.; Jiménez, C.; Eriksson, P.; Dupuy, E.; Amraoui, L.E.; Ekström, M.; Frisk, U.; Murtagh, D.; et al. Odin/SMR limb observations of stratospheric trace gases: Level 2 Processing of ClO, N_2O, HNO_3, and O_3. *J. Geophys. Res. Atmos.* **2005**, *110*, doi:10.1029/2004JD005741.
84. Pumphrey, H.C.; Bühler, S. Instrumental and spectral parameters: Their effort on and measurement by microwave limb sounding of the atmosphere. *J. Quant. Spectrosc. Radiat. Transf.* **2000**, *64*, 421–437.
85. Buehler, S.A.; Verdes, C.L.; Tsujimaru, S.; Kleinböhl, A.; Bremer, H.; Sinnhuber, M.; Eriksson, P. Expected performance of the superconducting submillimeter-wave limb emission sounder compared with aircraft data. *Radio Sci.* **2005**, *40*, 1–13.
86. Vogt, P. Charakterisierung des ballongetragenen Heterodynspektrometers TELIS und erste Atmosphärische Messungen. Unpublished dissertation, 2013.
87. Cortesi, U.; Lambert, J.C.; De Clercq, C.; Bianchini, G.; Blumenstock, T.; Bracher, A.; Castelli, E.; Catoire, V.; Chance, K.V.; De Mazière, M.; et al. Geophysical validation of MIPAS-ENVISAT operational ozone data. *Atmos. Chem. Phys.* **2007**, *7*, 4807–4867.
88. Steck, T.; von Clarmann, T.; Fischer, H.; Funke, B.; Glatthor, N.; Grabowski, U.; Höpfner, M.; Kellmann, S.; Kiefer, M.; Linden, A.; et al. Bias determination and precision validation of ozone profiles from MIPAS-Envisat retrieved with the IMK-IAA processor. *Atmos. Chem. Phys.* **2007**, *7*, 3639–3662.
89. Ochiai, S.; Kikuchi, K.; Nishibori, T.; Manabe, T.; Ozeki, H.; Mizobuchi, S.; Irimajiri, Y. Receiver performance of the Superconducting Submillimeter-Wave Limb-Emission Sounder (SMILES) on the International Space Station. *IEEE Trans. Geosci. Remote Sens.* **2013**, *51*, 3791–3802.
90. Sugita, T.; Kasai, Y.; Terao, Y.; Hayashida, S.; Manney, G.L.; Daffer, W.H.; Sagawa, H.; Suzuki, M.; Shiotani, M.; Walker, K.A.; et al. HCl and ClO profiles inside the Antarctic vortex as observed by SMILES in November 2009: Comparisons with MLS and ACE-FTS instruments. *Atmos. Meas. Tech.* **2013**, *6*, 3099–3113.
91. Livesey, N.; Van Snyder, W.; Read, W.; Wagner, P. Retrieval algorithms for the EOS Microwave Limb Sounder (MLS). *IEEE Trans. Geosci. Remote Sens.* **2006**, *44*, 1144–1155.
92. Jiang, Y.B.; Froidevaux, L.; Lambert, A.; Livesey, N.J.; Read, W.G.; Waters, J.W.; Bojkov, B.; Leblanc, T.; McDermid, I.S.; Godin-Beekmann, S.; et al. Validation of Aura Microwave Limb Sounder Ozone by ozonesonde and lidar measurements. *J. Geophys. Res. Atmos.* **2007**, *112*, doi:10.1029/2007JD008776.
93. Pumphrey, H.C.; Filipiak, M.J.; Livesey, N.J.; Schwartz, M.J.; Boone, C.; Walker, K.A.; Bernath, P.; Ricaud, P.; Barret, B.; Clerbaux, C.; et al. Validation of middle-atmosphere carbon monoxide retrievals from the Microwave Limb Sounder on Aura. *J. Geophys. Res. Atmos.* **2007**, *112*, doi:10.1029/2007JD008723.
94. Froidevaux, L.; Jiang, Y.B.; Lambert, A.; Livesey, N.J.; Read, W.G.; Waters, J.W.; Browell, E.V.; Hair, J.W.; Avery, M.A.; McGee, T.J.; et al. Validation of Aura Microwave Limb Sounder stratospheric ozone measurements. *J. Geophys. Res. Atmos.* **2008**, *113*, doi:10.1029/2007JD008771.
95. Froidevaux, L.; Jiang, Y.B.; Lambert, A.; Livesey, N.J.; Read, W.G.; Waters, J.W.; Fuller, R.A.; Marcy, T.P.; Popp, P.J.; Gao, R.S.; et al. Validation of Aura Microwave Limb Sounder HCl measurements. *J. Geophys. Res. Atmos.* **2008**, *113*, doi:10.1029/2007JD009025.
96. Livesey, N.J.; Filipiak, M.J.; Froidevaux, L.; Read, W.G.; Lambert, A.; Santee, M.L.; Jiang, J.H.; Pumphrey, H.C.; Waters, J.W.; Cofield, R.E.; et al. Validation of Aura Microwave Limb Sounder O_3 and CO observations in the upper troposphere and lower stratosphere. *J. Geophys. Res. Atmos.* **2008**, *113*, doi:10.1029/2007JD008805.

97. Jégou, F.; Urban, J.; de La Noë, J.; Ricaud, P.; Le Flochmoën, E.; Murtagh, D.P.; Eriksson, P.; Jones, A.; Petelina, S.; Llewellyn, E.J.; et al. Technical Note: Validation of Odin/SMR limb observations of ozone, comparisons with OSIRIS, POAM III, ground-based and balloon-borne instruments. *Atmos. Chem. Phys.* **2008**, *8*, 3385–3409.
98. Rodgers, C.D.; Connor, B.J. Intercomparison of remote sounding instruments. *J. Geophys. Res. Atmos.* **2003**, *108*, doi:10.1029/2002JD002299.
99. Von Clarmann, T. Validation of remotely sensed profiles of atmospheric state variables: Strategies and terminology. *Atmos. Chem. Phys.* **2006**, *6*, 4311–4320.
100. Ridolfi, M.; Ceccherini, S.; Carli, B. Optimal interpolation method for intercomparison of atmospheric measurements. *Opt. Lett.* **2006**, *31*, 855–857.
101. Aires, F. Measure and exploitation of multisensor and multiwavelength synergy for remote sensing: 1. Theoretical considerations. *J. Geophys. Res. Atmos.* **2011**, *116*, doi:10.1029/2010JD014701.
102. Landgraf, J.; Hasekamp, O.P. Retrieval of tropospheric ozone: The synergistic use of thermal infrared emission and ultraviolet reflectivity measurements from space. *J. Geophys. Res. Atmos.* **2007**, *112*, doi:10.1029/2006JD008097.
103. Natraj, V.; Liu, X.; Kulawik, S.; Chance, K.; Chatfield, R.; Edwards, D.P.; Eldering, A.; Francis, G.; Kurosu, T.; Pickering, K.; et al. Multi-spectral sensitivity studies for the retrieval of tropospheric and lowermost tropospheric ozone from simulated clear-sky GEO-CAPE measurements. *Atmos. Environ.* **2011**, *45*, 7151–7165.
104. Cuesta, J.; Eremenko, M.; Liu, X.; Dufour, G.; Cai, Z.; Höpfner, M.; von Clarmann, T.; Sellitto, P.; Foret, G.; Gaubert, B.; et al. Satellite observation of lowermost tropospheric ozone by multispectral synergism of IASI thermal infrared and GOME-2 ultraviolet measurements over Europe. *Atmos. Chem. Phys.* **2013**, *13*, 9675–9693.